3D coseismic surface displacements from historical aerial photographs of the 1987 Edgecumbe earthquake, New Zealand

Jaime Elizabeth Delano[1], Timothy Stahl[1], Andrew Howell[2], and Kate Clark[3]

[1]Univeristy of Canterbury
[2]University of Canterbury
[3]GNS Science

November 23, 2022

Abstract

Earthquake surface deformation provides key constraints on the geometry, kinematics, displacements, and complexity of fault rupture. However, deriving these precise characteristics from past earthquakes is complicated by a lack of detailed knowledge of landforms before the earthquake and how the landform has since been modified. The 1987 M_w 6.6 Edgecumbe earthquake in the northern Taupō volcanic zone in New Zealand represents a moderate-magnitude earthquake with complicated surface rupture that occurred before widespread high-resolution topographic data were available. We use historical aerial photos to build pre- and post-earthquake digital surface models using structure-from-motion techniques. By differencing the two surface models, we more definitively measure discrete and distributed deformation from this earthquake and compare the effectiveness of the technique to traditional field- and lidar-based studies. We identified most fault traces recognized by field mapping in 1987, mapped new traces not recorded in the field, and take denser, detailed remote slip measurements with a vertical separation resolution of ~0.3 m. Our maximum and average vertical separation measurements on the Edgecumbe fault trace (2.5 ± 0.3 m and 1.2 m, respectively), are similar to field-based maximum and recalculated averages of 2.4 m and 1.1 m, respectively. Importantly, this technique is able to discern between new fault scarps and pre-existing fault scarps better than field techniques or lidar-based measurements alone. Results from this approach can be used to refine estimated subsurface fault geometries and slip distributions at depth, and here is used to investigate potential magmatic-tectonic stress trigging in the northern Taupō volcanic zone.

Hosted file

`delano et al edgecumbe supp_file.docx` available at https://authorea.com/users/541535/articles/600653-3d-coseismic-surface-displacements-from-historical-aerial-photographs-of-the-1987-edgecumbe-earthquake-new-zealand

3D coseismic surface displacements from historical aerial photographs of the 1987 Edgecumbe earthquake, New Zealand

J. E. Delano[1], T. A. Stahl[1], A. Howell[1,2] and K. Clark[2]

[1]School of Earth and Environment, University of Canterbury, Christchurch, New Zealand

[2]GNS Science, PO Box 30368, Lower Hutt, New Zealand

Corresponding author: Jaime Delano (jaimedelano@gmail.com)

Key Points:

- Historical aerial photos can be used to generate pre- and post-earthquake surface models for measuring displacement.
- This method performs at least as well as field surveys, and better captures single event displacements to constrain slip behavior.
- The Edgecumbe earthquake is important for understanding low dip-angle normal fault ruptures and possibly magma-tectonic interactions.

Key words: Normal fault, earthquake, remote sensing, structure-from-motion, Taupō volcanic zone, tectonics, aerial photographs, airphotos

Abstract

Earthquake surface deformation provides key constraints on the geometry, kinematics, displacements, and complexity of fault rupture. However, deriving these precise characteristics from past earthquakes is complicated by a lack of detailed knowledge of landforms before the earthquake and how the landform has since been modified. The 1987 M_w 6.6 Edgecumbe earthquake in the northern Taupō volcanic zone in New Zealand represents a moderate-magnitude earthquake with complicated surface rupture that occurred before widespread high-resolution topographic data were available. We use historical aerial photos to build pre- and post-earthquake digital surface models using structure-from-motion techniques. By differencing the two surface models, we more definitively measure discrete and distributed deformation from this earthquake and compare the effectiveness of the technique to traditional field- and lidar-based studies. We identified most fault traces recognized by field mapping in 1987, mapped new traces not recorded in the field, and take denser, detailed remote slip measurements with a vertical separation resolution of ~0.3 m. Our maximum and average vertical separation measurements on the Edgecumbe fault trace (2.5 ± 0.3 m and 1.2 m, respectively), are similar to field-based maximum and recalculated averages of 2.4 m and 1.1 m, respectively. Importantly, this technique is able to discern between new fault scarps and pre-existing fault scarps better than field techniques or lidar-based measurements alone. Results from this approach can be used to refine estimated subsurface fault geometries and slip distributions at depth, and here is used to investigate potential magmatic-tectonic stress trigging in the northern Taupō volcanic zone.

Plain Language Summary

Understanding earthquake behavior relies heavily on information about how past earthquakes affected the surface landscape. Detailed information about the surface topography before the earthquake is often limited, creating challenges for accurately measuring earthquake surface slip. Aerial photos are widely available and can be used to create 3D surface models in places where other pre- or post-earthquake topographic information is lacking. We use historical aerial photos to make 3D models of the surface topography before and after the 1987 Edgecumbe earthquake in New Zealand. We then created a difference map from those two models in order to identify and measure how the earthquake changed the landscape, and compared our results to previous measurements. We found that this method generally works as well as field methods for identifying and measuring fault movement, and has some advantages over other techniques. In particular, this approach can separate deformation from individual earthquakes, which had previously been a challenge. The results refine our understanding of the fault below the surface, relationships to the surrounding fault and volcanic system, and better characterize seismic hazard both here and in other similar geologic settings.

1 Introduction

Historical earthquakes provide one of the best opportunities to characterize surface ruptures and the hazards posed by coseismic deformation (e.g., Wesnousky, 2008; Youngs et al., 2003). Empirical scaling laws and fault displacement hazard analysis are largely based on inventories of surface-deforming events that have occurred over the last ~150 years. However, accurately deriving surface rupture and displacement characteristics from historical earthquakes can be challenging, particularly for events that occurred before satellite- and lidar-based datasets became widely available. In regions with infrequent earthquakes, high relief scarps, and/or low erosion rates, modern high-resolution topography can capture many characteristics of older historical earthquake ruptures (e.g., DuRoss et al., 2019; Middleton et al., 2016; Nissen et al., 2014; Shao et al., 2020). Elsewhere, reconnaissance mapping (if undertaken at the time) or sparse paleoseismic trenches may be the only records of historical ruptures (e.g., Ambraseys, 1963; Henderson, 1933; Kelsey et al., 1998; Schermer et al., 2004). The details of coseismic deformation in these dynamic landscapes may be lost over time to erosion, vegetation growth, or anthropogenic modification. For many historical earthquakes, assumptions about pre-earthquake topography and landscape modification between the event timing and data collection add significant uncertainties to reconstructions of displacements and rupture extent.

Historical and modern aerial photographs occupy a useful niche for studying earthquakes because they span long periods of time (70+ years), often with repeat surveys. With more recent advances in photogrammetry techniques, legacy aerial photographs can be used to generate additional pre and post-earthquake topographic data to supplement lidar, satellite, and field-based data (e.g., Howell et al., 2020; Zhou et al., 2016). This means that high-resolution 2D and 3D displacement fields, typically only achievable for recent ruptures with modern techniques like differential lidar or InSAR, can theoretically be produced for any earthquake where pre- and post-event images are available. Surface displacements derived from aerial imagery can serve as a compromise between resolution, coverage, and availability compared to other remote sensing or field data.

Aerial images present some advantages over other remote sensing or measurement techniques and have broad applicability over a variety of geologic settings. Post-earthquake field surveys, including levelling lines, fault rupture mapping, and offset measurements, can capture fine-scale and ephemeral features (e.g., Beanland et al., 1989; Blick & Flaherty, 1989; DuRoss et al., 2019; Koehler et al., 2021; Litchfield et al., 2018). However, such surveys may miss subtle, broader-scale deformation, can be hindered by time, weather, and access, and have uncertainties that are difficult to quantify. Lidar data across earthquake ruptures provide high-resolution, geometrically accurate data in 3D (e.g., Duffy et al., 2013; Oskin et al., 2012) and the bare-earth capabilities outperform image-based methods in vegetated areas (Ekhtari & Glennie, 2018). Lidar is also expensive to collect and typically requires reconnaissance to define the area of interest, so coverage over the full deformation field may be incomplete, such as for the 2016 Kaikōura earthquake (e.g., Litchfield et al., 2018). Pre-earthquake topography is commonly unavailable so is often assumed or gathered from other sources (e.g., Lajoie et al., 2019). Satellite-based data (InSAR and satellite images) have the advantage of frequent data collection, but are limited to the last few decades. Satellite imagery resolution may be too coarse for smaller displacements, and InSAR suffers from data loss where strain is high near the fault trace (e.g., Elliott et al., 2016).

This study focuses on the 1987 Edgecumbe earthquake as an example of surface rupture that can be comprehensively reconstructed with pre and post-earthquake aerial imagery, filling the gap between the historical event timing (1987) and lidar collection in 2006 and 2011. We use historical aerial photos of the Rangitāiki Plains in the North Island of New Zealand (Fig. 1) and photogrammetry software to generate pre- and post-earthquake digital surface models (DSMs) and orthophotos from the 1987 Edgecumbe earthquake. Most existing studies that use similar remote sensing techniques focus on larger magnitude (M_w 7+) earthquakes where slip is more easily resolved (e.g., Barnhart et al., 2019; Howell et al., 2020; Zhou et al., 2016). The M_w 6.6 Edgecumbe earthquake, conversely, represents a moderate magnitude earthquake with <2 m average slip (Beanland et al., 1989), and therefore tests the limits of this technique with a final

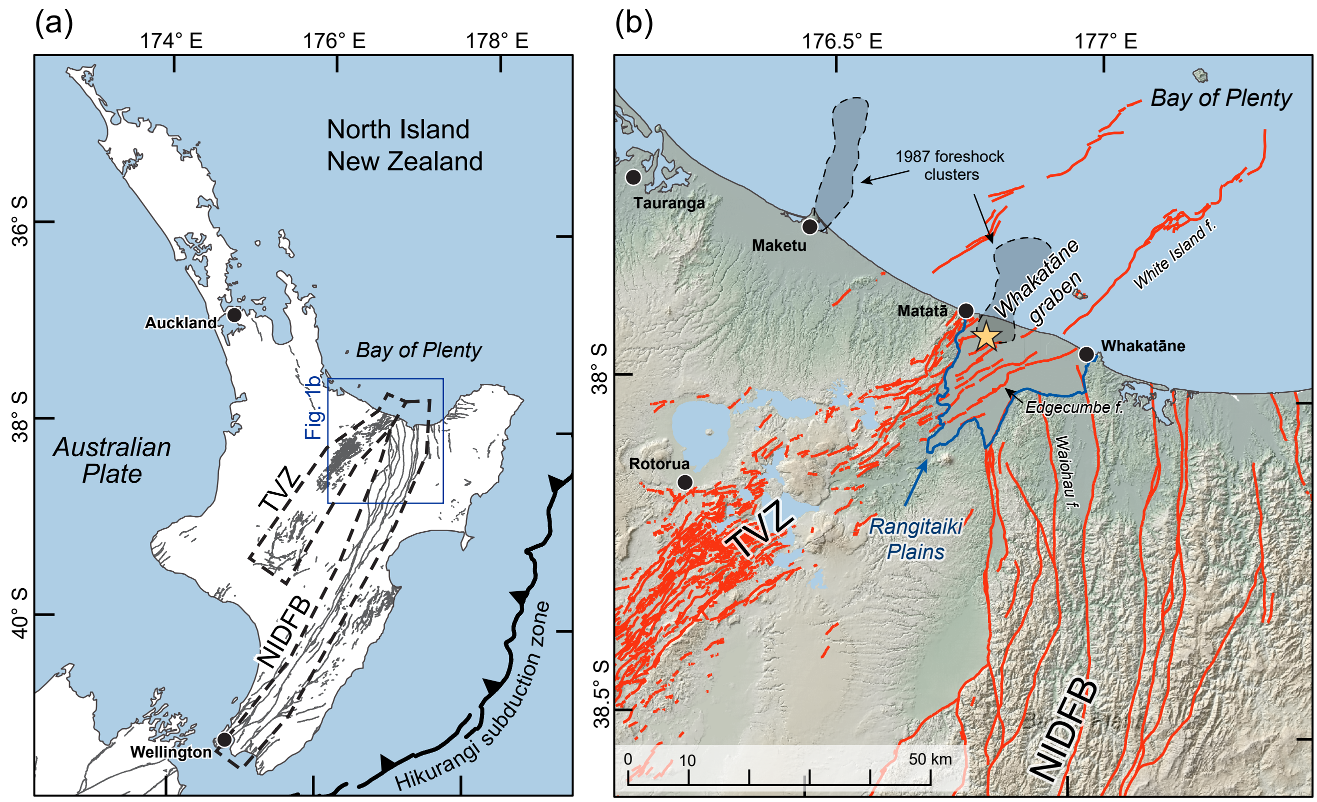

Figure 1: Tectonic setting of the 1987 Edgecumbe earthquake investigated in this study. (a) The Edgecumbe earthquake occurred in the northern Taupō volcanic zone (TVZ), a zone of backarc extension in the Australian plate above the Hikurangi Subduction Zone. Active faults in grey (Langridge et al., 2020). (b) Most of the Edgecumbe earthquake surface rupture occurred within the Rangitāiki Plains, which lies on the onshore Whakatāne graben at the intersection of the TVZ and North Island dextral fault belt (NIDFB). Simplified onshore active faults in red (Langridge et al., 2016); only graben-bounding faults are shown offshore (Lamarche et al., 2006). Epicenter (star) is from Anderson and Webb (1989); foreshocks are from Smith and Oppenheimer (1989).

topographic product resolution that approaches the scale of surface displacement. The existence of several different displacement datasets (lidar, levelling surveys, and field measurements) allow for robust sensitivity tests of our method and provide realistic constraints on the limits of using historical aerial photographs to characterize coseismic slip and fault behavior at depth. The new dataset provides a more complete picture of fault rupture hazards from moderate-magnitude normal-fault earthquakes as well as insights into possible interactions between magmatic and tectonic processes in the Taupō volcanic zone and elsewhere.

2 Geologic setting

The 1987 Edgecumbe earthquake occurred within the Whakatāne graben at the northern end of the onshore Taupō rift on the North Island of New Zealand (Fig. 1) (Beanland et al., 1989). The Taupō rift (or Taupō fault belt) is a region of localized normal faults in the Taupō volcanic zone (TVZ), the continental volcanic arc associated with the Hikurangi subduction zone (Fig. 1) (e.g., Wilson et al., 1995). GNSS data show the northernmost TVZ is extending at a rate of ~15 mm/yr (Wallace et al., 2004).

The structure of the Whakatāne graben is primarily controlled by the northwest-dipping Edgecumbe-White Island fault; the White Island fault is the offshore continuation of the onshore Edgecumbe fault (Fig. 1b) (Lamarche et al., 2006). The Edgecumbe fault accommodates primarily normal motion and displaces basement greywacke overlain by a succession of alluvial, wetland, and marine sediments, erupted rocks, and reworked volcanic deposits that make up the Rangitāiki Plains (Fig. 1b) (Beanland et al., 1990; Ota et al., 1988). The eastern margin of the onshore Whakatāne graben is located within the Rangitāiki Plains and coincides with a transitional zone where the dominantly strike-slip North Island dextral fault system (also referred to as North Island dextral fault belt and North Island fault system) and the extensional Taupō Rift begin to intersect (Fig. 1) (Mouslopoulou et al., 2007). The western margin of the onshore Whakatāne graben is thought to be largely controlled by the east-dipping Matatā fault (e.g., Begg & Mouslopoulou, 2010; Ota et al., 1988). Active volcanoes are located in the northeast (offshore) and southwest (onshore) sections of the graben, and off-axis magma chamber inflation has been inferred immediately west of Matatā (Hamling et al., 2016). Taken together, previous studies demonstrate that the Edgecumbe earthquake occurred in a relatively simple graben within a complex tectonic setting (e.g., Wilson & Rowland, 2016).

The M_w 6.6 Edgecumbe earthquake initiated on 2 March 1987 within the Whakatāne graben and produced dominantly normal slip (Fig. 1b) (H. Anderson & Webb, 1989; Beanland et al., 1989, 1990; Darby, 1989). Poor instrument distribution leads to some uncertainty in the hypocenter and centroid locations and rupture mechanism, but the most recent estimates indicate a relatively shallow centroid depth (6 ± 1 km) on a gently dipping fault plane (32° +5/-10°) striking southwest (229 ± 10°) with dominantly normal rake (-113 ± 12°) (Webb & Anderson, 1998). Seismological studies interpreted that the mainshock initiated near the northern, basal edge of the Edgecumbe fault plane and rupture propagated unilaterally towards the southwest (Webb and Anderson 1998; Anderson and Webb 1989).

The mainshock was preceded by foreshocks (starting 21 February, 1987) in two northeast-southwest-trending clusters: one in the Whakatāne graben between Matatā and Thornton and the other farther northwest near Maketu (Fig. 1b) (Smith & Oppenheimer, 1989).

The Edgecumbe earthquake aftershocks were primarily between 4–6 km depth and were nearly all <8 km deep, which together indicate a brittle ductile boundary at 6–8 km depth near the Rangitāiki Plains (Robinson, 1989).

The 1987 Edgecumbe earthquake ruptured a number of pre-existing, but previously unrecognized faults in the onshore Whakatāne graben (Beanland et al., 1989). Following the 1987 earthquake, field-based surveys conducted fault trace mapping, discrete horizontal and vertical displacement measurements along surface ruptures, limited short (~40-m-long) topographic profile measurements, and levelling surveys along the major roads (Beanland et al., 1989; Blick & Flaherty, 1989). The earthquake produced many short surface ruptures on widely spaced faults with relatively high measured slip-to-fault-length ratios compared to other normal fault earthquakes recorded globally (Beanland et al., 1990). Most of the slip occurred on the Edgecumbe fault, the inferred primary structure where the mainshock initiated (Beanland et al., 1989). The field-based Edgecumbe fault measurements yielded a maximum normal dip slip of 3.1 m (2.5 m throw and 1.3 m heave) along a 7-km-long trace, with no evidence of strike-slip motion (Beanland et al., 1989). Repeat levelling surveys along major roads identified that ~10% of coseismic displacement values were accommodated as afterslip in the months following the earthquake (Blick & Flaherty, 1989). Farther-field coseismic displacement estimates, however, are limited in extent and complicated by sparse pre-earthquake survey reference benchmarks that were displaced during the earthquake. Levelling surveys by Blick & Flaherty (1989) noted no uplift within the Edgecumbe fault footwall, although the surveys lacked an absolute reference frame and transects crossed the main fault at an oblique angle in a zone of smaller displacements.

3 Methods

We used pre- and post-earthquake aerial photographs to create SfM-based digital surface models (DSMs) and orthophoto mosaics of the Rangitāiki Plains. The primary new data presented in this study are these DSMs and a coseismic vertical difference model of the Edgecumbe earthquake derived from them. These photogrammetry-based datasets provided means to map surface rupture, measure coseismic vertical separation, and estimate near-fault horizontal displacement. Finally, we combined our remote measurements to create the most informed elastic dislocation model of the 1987 Edgecumbe earthquake that synthesizes fault information generated in the last few decades.

3.1 Aerial images

An ideal photoset for photogrammetric or SfM-based modelling is high-resolution, has ample (~60%) overlap between photos (e.g., Abdullah et al., 2013; Krauss, 1993), covers an extent beyond the area of interest (e.g., Reitman et al., 2015), and is taken with the same camera and specifications with no changes in lighting or the subject (e.g., Bemis et al., 2014). For aerial photos, this generally implies that photos should be captured at a low flight altitude (high image resolution) and all photos should be captured with the same camera, lens, and settings. Assuming a constant flight speed, image overlap is a function of image capture rate and the lens focal length; longer focal lengths have a narrower view angle and thus less overlap between images for the same capture rate. Some historical photo sets comprise more than one flight that can include changes in lighting (different sun angle), vegetation cover (different seasons), and changes to the built or agricultural environment. Thus, the ideal pre- or post-event photo sets should minimize the number of flights and overall elapsed time as well as differences in sunlight and season to reduce changes caused by non-tectonic processes. SfM model quality may improve when camera calibration information, detailed photo survey specifications, and georeference information are available.

We generated SfM-based models using historical photosets from 1972-1975 and March 1987 to build pre- and post-earthquake DSMs, respectively (see Open Data). Both photosets were scanned using a photogrammetric scanner into digital files at 1800 dpi. The post-earthquake photo set (survey SN8732) consists of 762 images taken with a 152 mm lens on a Zeiss RMK camera at an altitude of ~5,000 feet (~1524 m). These photos were collected within one month of the 2 March Edgecumbe mainshock over four flight dates. The original printed photos were 23 cm square format and were scanned to approximately 18,000 x 16,900 pixels. This post-earthquake aerial survey was purpose-collected for studying the 1987 Edgecumbe earthquake and therefore contains high-resolution photographs (low flight altitude) with large overlap between adjacent photos due to a relatively small camera focal length and closely timed photo interval.

The pre-earthquake photo set (survey SN3580) is composed of 611 images taken with a 210 mm lens on an AT119 Wild RC8 camera at an altitude of ~17,500 feet (~5334 m). The entire photoset represents nine flight dates across different seasons and three calendar years, which leads to additional noise and uncertainty in generating the final model (elaborated on below). The original printed photos were 18 cm square images and were scanned to approximately 14,500 x 13,500 pixels.

Only one photoset was collected immediately after the earthquake (SN8732), but several photoset options exist for the pre-earthquake model. We chose SN3580 because although some collection aspects are not ideal (e.g., long collection time window) it had the highest likelihood of success due to the (i) large spatial extent across the entire onshore Whakatāne graben, (ii) single camera and lens used throughout the entire survey, (iii) smaller camera focal length, and (iv) lowest flight altitude compared to other photosets. Minimizing time between the pre- and post-earthquake imagery is another important consideration to reduce non-tectonic changes to the landscape; other photosets taken more recently than SN3580 (i.e., between 1974 and 1987) likely capture fewer non-tectonic and anthropogenic surface changes. These other photosets, however, lack the resolution required to generate a DSM with sub-meter vertical resolution due to higher flight altitudes, suboptimal camera specifications, poor photo overlap, and limited spatial extent.

3.2 Pre- and post-earthquake model generation

The SfM models and derived products (e.g., dense point clouds, DSMs, and orthophoto mosaics) were generated using Agisoft Metashape Pro v1.7. We included camera calibration information such as photo fiducial locations and precise camera focal length for both sets of historical photos to improve photo alignment. Other distortion parameters listed in the calibration file were effectively zero at the scale of the photo scan—including these in the models had no noticeable effect on the final DSM.

Some studies suggest that using down-sampled, reduced resolution scanned images (50% original resolution) may improve initial photo alignment by distributing tie points more evenly (Lu et al., 2021). We found that reducing photo resolution here, while keeping other parameters the same, produced poorer model results compared to the full resolution scans. This may be a result of the relatively low relief landscape on the Rangitāiki Plains, differences in photogrammetric software, or high degree of anthropogenic modification between collection times. For our dataset, we found that increasing the number of key points and tie points above the default value (to 60,000 and 10,000, respectively) substantially improved the initial photo alignment.

Both pre- and post-earthquake SfM models were georeferenced using coordinates derived from the 2011 lidar point clouds (see Open Data). First, we identified cultural markers that were visible and unchanged in the pre-earthquake photos, post-earthquake photos, and 2011 lidar survey orthoimages. These landmarks are typically bridges (e.g., at the intersection of a concrete deck and the centerline), unique road intersections, statue bases, or fence corners. These features are unlikely to have been moved or changed over the decades between photo and lidar datasets because they are permanent structures or long-lived property boundaries. When choosing control point locations, we avoided irregular surfaces, which could introduce elevation uncertainty. The control point coordinates were extracted from the point cloud data rather than the georeferenced lidar survey orthoimages to reduce the potential of location uncertainty from image warping. The choice of using lidar-based control points is multifold: (i) the lidar dataset has the widest extent and is the densest georeferenced dataset available remotely for this region, (ii) traditional survey benchmarks, such as those used for the New Zealand Transportation Agency are not visible in aerial images, (iii) using a common reference between photos removes possible long-term changes due to continuous, slow movement (e.g., plate motions or magma inflation), and (iv) the lidar-referenced SfM models can be easily compared to the more recent lidar topography to identify locations with poor photo alignment, increased model distortion, or other poor model fits. We use a conservative estimated control point location accuracy of 0.5 m in Agisoft Metashape Pro to account for lidar point cloud density and air photo resolution.

Since georeferenced coordinates originate from 2011, several decades after the 1987 earthquake and the pre-earthquake photosets, we placed control points so as to minimize the influence of tectonic and other landscape changes. Most control points reside along the Rangitāiki Plains margin, in the surrounding hills, or in regions with no recorded deformation in the Edgecumbe fault footwall (e.g., Whakatāne) (Blick & Flaherty, 1989). This means that control in the interior of the graben, where subsidence was widespread, is sparse. This implies that the resulting models, particularly in the pre-earthquake model and the graben center on both models, may include absolute spatial inaccuracies.

We found that including "check points" (an Agisoft-software-specific term) during the alignment steps improved the photo alignment and reduced some artifacts. These points identify common pixels between photos but do not influence georeferencing, and help reduce distortion between photos. Model improvements from these check points were greatest for the pre-earthquake photoset where harsher vignetting, larger time gaps between photos, and less ideal flight and camera specifications caused sharp, artificial topographic steps between flight lines. In total, we placed 21 control points and 95 check points in the pre-earthquake model and 29 control points and zero check points in the post-earthquake model (Tables S1-S2).

The final outputs from the pre- and post-earthquake SfM models include DSMs, generated from the dense point cloud within Agisoft Metashape Pro, and orthorectified photomosaics (orthophoto mosaics). We subtracted the pre-earthquake DSM from the post-earthquake DSM to produce a 2-m vertical difference model, which was the primary data used to map coseismic deformation (Fig. 2a).

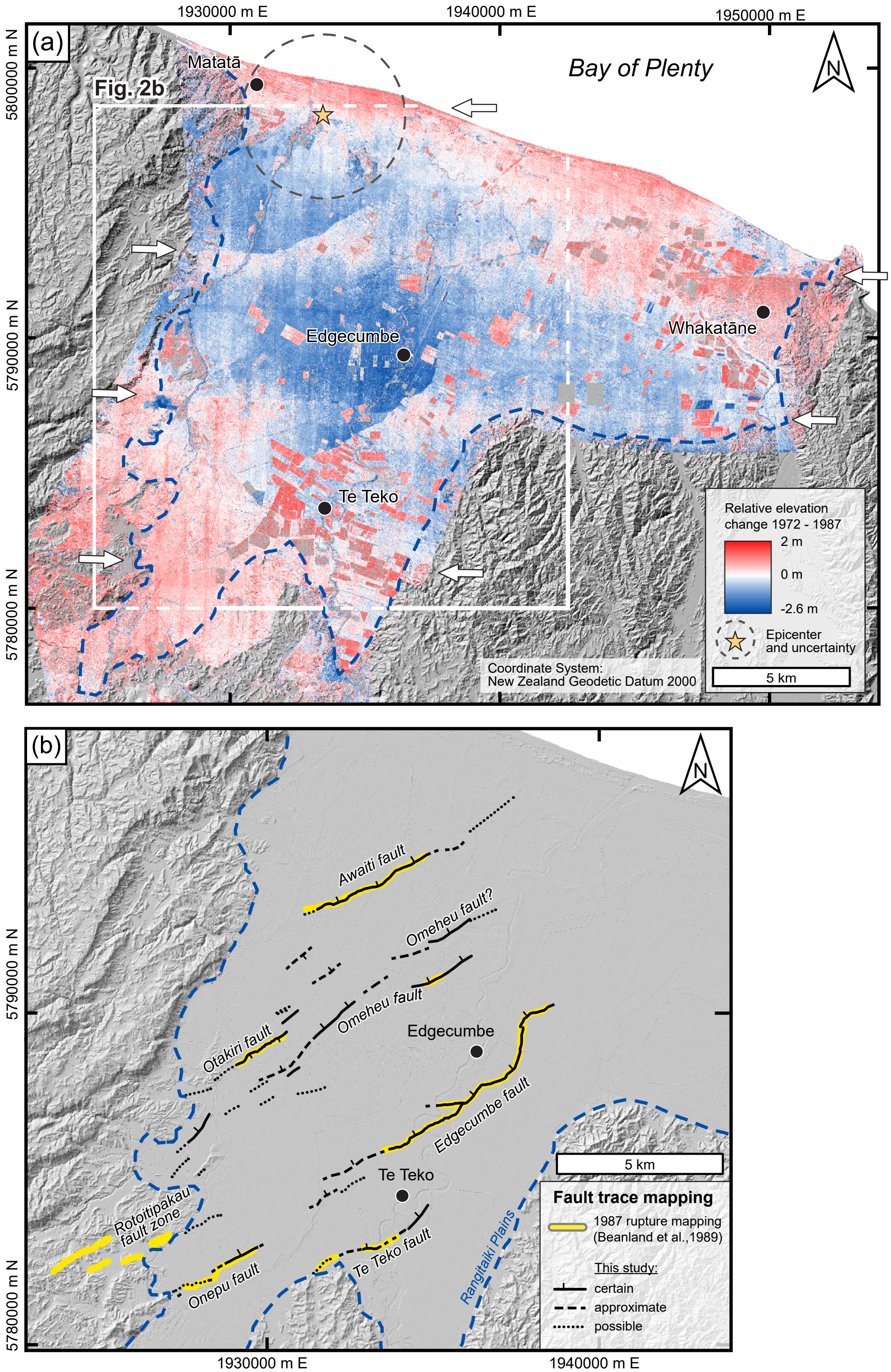

Figure 2: Results of SfM-based topographic differencing and coseismic fault trace mapping. (a) Vertical difference model generated by subtracting pre- and post-earthquake SfM-based DSMs. The relative elevation changes include artifacts from poor photo overlap between flight lines (east-west lines, highlighted by white arrows) and multiple survey dates, but captures shorter-scale displacements along discrete faults and broader patterns of subsidence. Epicenter is from Anderson and Webb (1989). (b) Edgecumbe earthquake surface rupture mapping from the vertical difference model compared to the trace mapping performed in 1987 by Beanland et al. (1989). All faults except the Rotoitipakau fault zone were identified in this study, and many small fault traces not identified in the field were visible in the vertical difference model.

3.3 Fault mapping

We identified surface ruptures from the 1987 Edgecumbe earthquake using the 2-m vertical difference model (Fig. 2). Mapped fault traces mark where there was a relatively linear, continuous (>100-m-long), and discrete change in vertical difference values. We investigated but ultimately ignored linear value changes (apparent scarps) that had persistent trends of exactly north-south or east-west because these result from seams between individual photos and flight lines. Each mapped scarp was checked against the pre- and post-earthquake photomosaics to identify if changes in cultural features or development, such as agricultural plots, could produce an artificial scarp. Scarps with distinct, sharp vertical difference value changes that clearly cross-cut otherwise continuous landforms were mapped as 'certain' fault traces. Where the vertical change location was less sharp and displacement occurred over a broader area, we mapped the scarp as an 'approximate' fault trace. If the displacement was very broadly distributed, very subtle, or difficult to distinguish, we mapped fault traces as 'possible'.

3.4 Measurements of vertical offsets across faults

We extracted swath profiles across the fault scarps from the vertical difference model to measure 1987 coseismic vertical separations. The initial 2 m vertical difference model was resampled to a 4 m grid size using a bilinear interpolation to reduce some of the high-frequency noise originating from the pre-earthquake DSM before extracting swath profile values.

Fault profile locations were chosen based on (i) visible surface displacement across a certain or approximate fault trace, (ii) relatively unchanged topography adjacent to the fault between the pre- to post-earthquake photosets, and (iii) ~250 m spacing along the fault trace, but with denser or less dense spacing depending on (i) and (ii). Finding locations to fit criterion (ii) proved to be the most difficult, because this region is heavily farmed and agricultural plots and property lines frequently follow or terminate near fault scarps. This leads to instances where vegetation growth or removal may influence the surface elevation on one side of the fault but not the other, leading to apparent vertical separation not caused by the 1987 earthquake.

At each profile location, we extracted vertical difference model values along 1-km-long, 30-m-wide swaths centered on and orthogonal to the mapped fault trace (locations in Fig. 3a) (for profile tool, see Howell, 2021). We then selected points on the up- and down-thrown sides of the fault that best represented the original planar surface topography. We omitted points from hedgerows, ditches, differential vegetation growth or removal (relative to the other side of the fault), roads, or buildings. With the remaining selected points, we fit lines to the hanging wall and footwall slopes and projected the lines to the scarp midpoint distance (Fig. 4). The final vertical separation value is the vertical distance between the two projected lines with one standard deviation. Other calculations of uncertainty, such as standard error, result in very low values (~0.05 m compared to ~0.5 m for standard deviation) due to the good linear fit and the large number of points being used. However, since the scatter in extracted vertical difference model values can reach up to 1 m vertically along the profile distance (see Fig. 4), we consider the use of standard deviation more conservative and appropriate. The above fault profile methods were repeated using the 2011 lidar 2 m DEM to compare to the coseismic SfM-based displacement measurements and 1987 field-based measurements.

Finally, to compare all measurement methods and changes in displacement along fault strike, we projected vertical separations from the SfM-based, lidar-based, and field-based

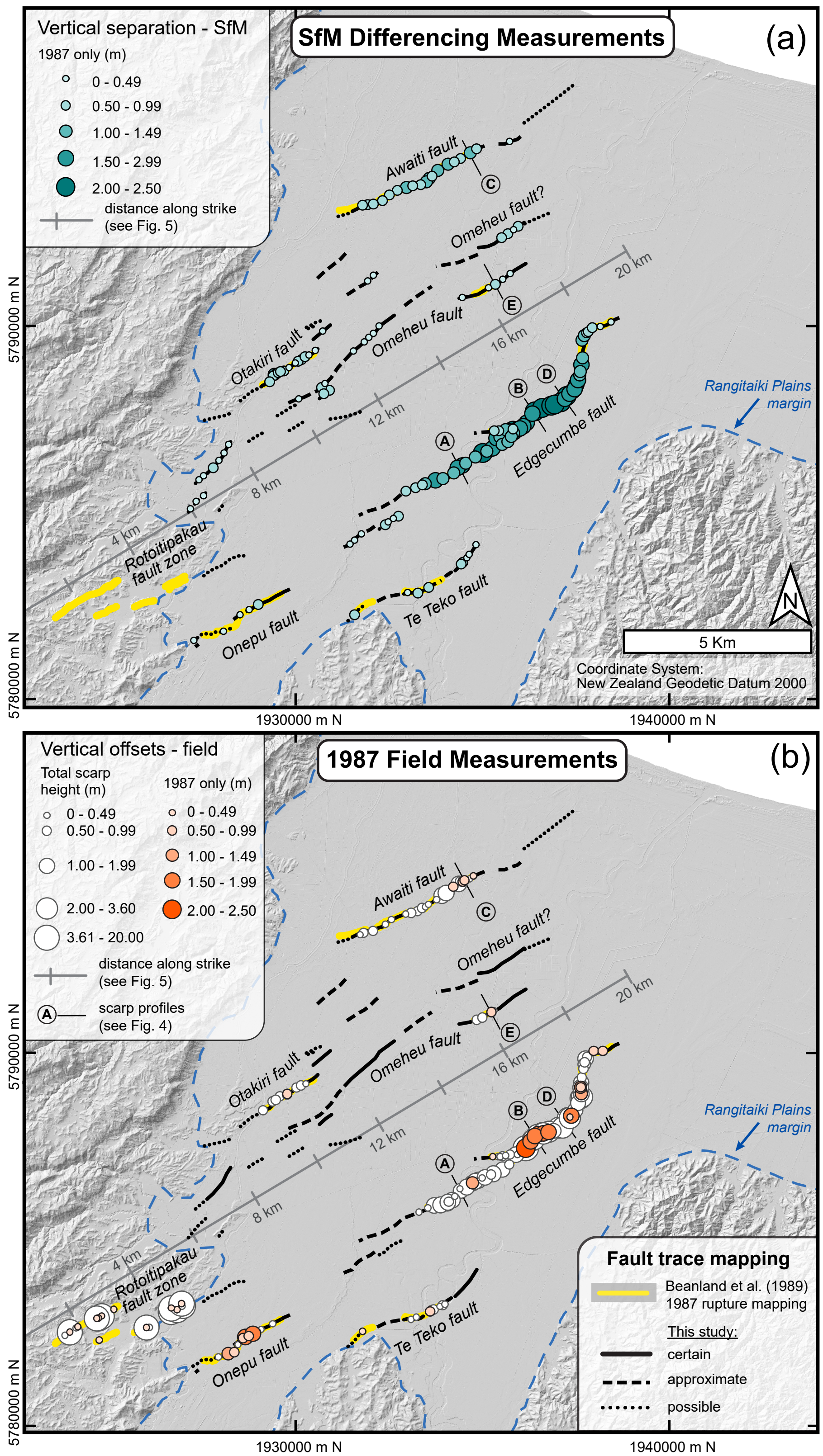

Figure 3: Results of field and SfM-based vertical separations in map view. (a) The SfM differencing method identifies single-event displacement rather than multi-event displacement. Distance along strike (grey line with tick marks) used in Fig. 5. (b) Field-based measurements could distinguish 1987-only offsets (orange circles) in select places. Total scarp offsets (white circles) may represent one event or multi-event displacement. Field offsets from Beanland et al. (1989). Scale and fault trace mapping is the same in (a) and (b).

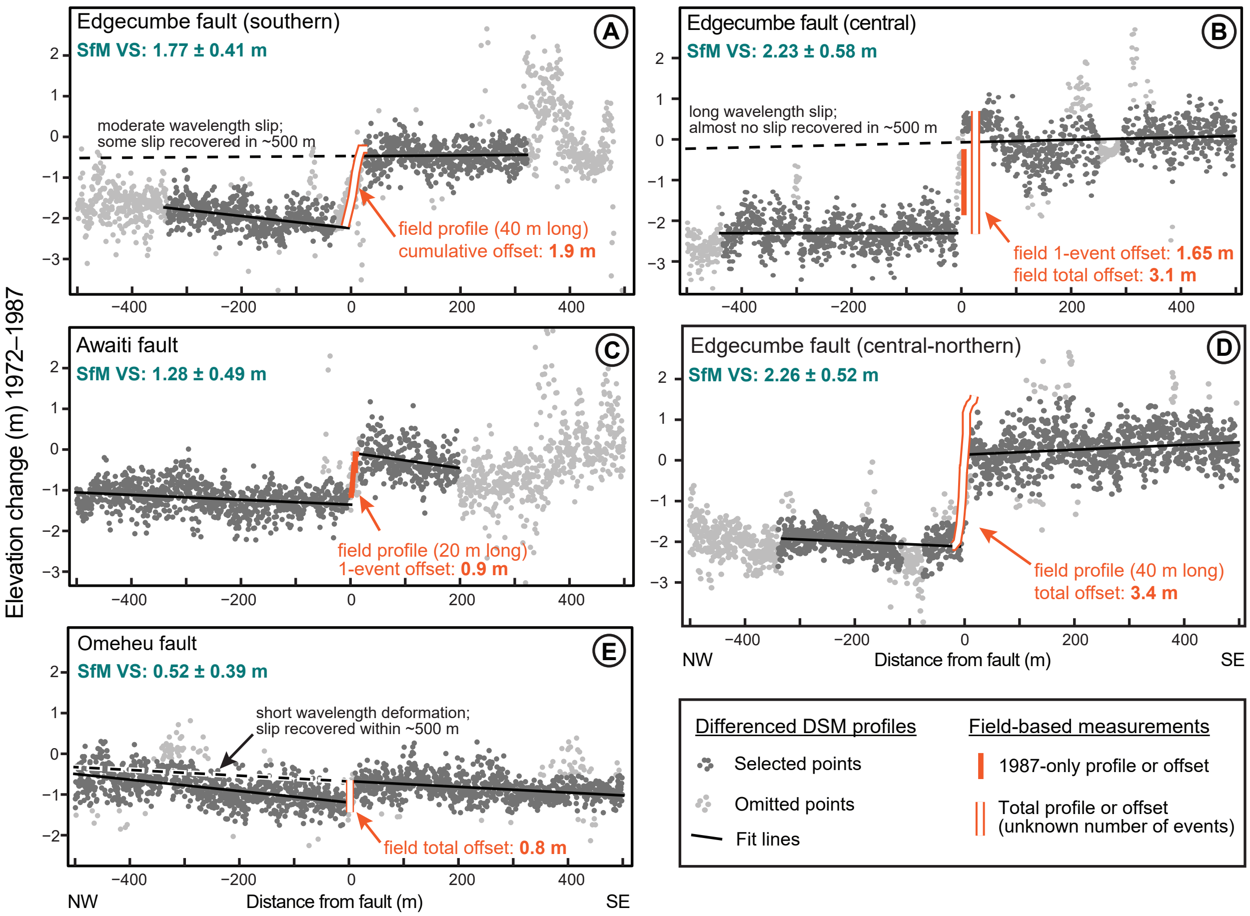

Figure 4: Examples of scarp profiles used in SfM-based vertical separation (VS) and field-based vertical offset measurements. Profiles A-E (locations in Fig. 3) extracted along a 1-km-long, 30-m-wide swath from the vertical difference model. SfM-based measurements better capture far-field displacement than field-based measurements, can distinguish single- from multi-event displacement, and can inform how deep slip extends at depth. Field profiles and offsets from Beanland et al. (1989).

measurements to central line that parallels the faults zone trend (azimuth 60°/240°) (projection line in Fig. 3).

3.5 Horizontal displacements and coseismic heave

Vertically differencing pre- and post-Edgecumbe earthquake DSMs captures a large portion of coseismic displacement since the earthquake produced dominantly normal slip. It does not, however, account for either lateral slip (strike-slip) or the horizontal component of normal slip (heave). No lateral slip was identified following the earthquake, but field surveys found significant extension across the Whakatāne graben (Beanland et al., 1989; Crook & Hannah, 1988). To compare horizontal displacement results from this study to field-based estimates, and to estimate total coseismic slip, we attempted 3D point cloud differencing using the iterative closest point algorithm (e.g., Nissen et al., 2012), 2D optical image correlation of the SfM-based orthomosaics (e.g., Leprince et al., 2007), and manual feature matching using georeferenced pre- and post-earthquake orthomosaics.

The 3D point cloud differencing (e.g., as in Howell et al., 2020) achieved poor results with the pre- and post-Edgecumbe earthquake datasets. We found that the relatively flat topography, sparse and small surface features (e.g., buildings and ditches) and high degree of non-tectonic surface change between photosets inhibited correlation between the pre- and post-earthquake point clouds. Similar problems were encountered with the 2D image correlation, with additional problems caused by different shadows from varying sun angles.

Finally, we measured horizontal movement by identifying fixed cultural features (e.g., livestock water troughs) visible in both the pre- and post-earthquake orthomosaics and manually drawing the displacement vector. This method was effective, but the resulting horizontal vectors are more sparsely distributed than continuous 3D point cloud or 2D image correlation methods. Additionally, they do not represent absolute displacements because we lack accurate independent pre-earthquake geographic control data. Relative horizontal movements over fairly short distances (<4 km), such as between the hanging wall and footwall of a fault, should be more accurate.

To estimate fault heave along the surface trace, we calculated the coseismic horizontal motion of the hanging wall relative to a fixed footwall. First, we made groups of horizontal displacement vectors (within ~1 km of each other) in the hanging wall and footwall (Fig. S1). Each vector group was averaged to give a single mean value. Then, each footwall average vector was subtracted from the corresponding hanging wall average vector to yield the average coseismic horizontal displacement of the hanging wall, relative to the footwall (Table S3). The resulting vectors along the central Edgecumbe fault are oriented ~90° to the fault trace; thus, we assume pure normal motion which is consistent with field based measurements (Beanland et al., 1989) and equate all horizontal motion to heave.

3.6 Elastic dislocation modelling methods

We create a simple elastic dislocation model to approximate the behavior of the 1987 Edgecumbe fault rupture at depth using Coulomb 3.3 (Toda et al., 2011). The model is constrained using the updated surface displacement information produced in this study as well as existing data on fault dip, hypocenter location, additional surface deformation data, and seismogenic crustal thickness. We use a Poisson's ratio of 0.25, and a Young's modulus of 8×10^5 bar, corresponding to a shear modulus (μ) of 3.3×10^{10} Pa. We also calculate stress changes on faults in the area of interest associated with possible inflation of a sill at depth (Hamling et al., 2016); during stress calculations, we assume a moderate coefficient of friction of 0.4 based on recommendations in Toda et al. (2011). The resulting preferred model represents the simplest, best-fitting elastic dislocation parameters (of those explored below) that can explain the observed surface deformation.

The top edge and strike of the modelled Edgecumbe fault are based on the surface deformation mapped in this study. Traces mapped as either certain or approximate on the primary Edgecumbe fault inform the fault length; we also infer a 0 km upper edge depth since the fault broke to the surface in 1987. This fault length likely includes a small portion of shallow, blind slip near the southern extent of the rupture, where field surveys did not indicate a fault trace but surface deformation was noted in this study.

While the Edgecumbe fault plane extends both to the north and south at depth (Mouslopoulou et al., 2008), we only model the slip that likely occurred due to the 1987 mainshock. The northern terminus of our modelled fault (and mapped surface trace) is located near the approximate intersection with the Waiohau fault of the North Island dextral fault system (Fig. 1) (Mouslopoulou et al., 2008). This junction may have impeded further fault rupture to the north during the 1987 event (Mouslopoulou et al., 2008), in which case, it is an appropriate location for the end of our modelled fault. Small amounts of slip at depth may have continued beyond the modelled southern extent of the Edgecumbe fault plane, but did not contribute significantly to surface deformation in 1987 and would not strongly change moment release estimates or patterns of surface deformation.

We vary basal depth within a range of plausible values, but assume the northern fault base intersects the approximate hypocenter of the 1987 mainshock. Hypocenter/epicenter and centroid locations are inconsistently reported and sometimes used interchangeably in the literature, and there are no strong constraints on either hypocenter depth or centroid latitude/longitude. We prefer models where: (1) the latitude and longitude of the earthquake epicenter (from H. Anderson and Webb, 1989) fall within or close to the lateral boundary of the modeled fault plane; and (2) the modeled fault extends from the surface to a depth greater than the seismological centroid depth. Body wave modeling suggests a centroid depth of 6 ± 1 km (Webb & Anderson, 1998). However, the true uncertainty on this depth may be greater than the formal value of 1 km once uncertainties in velocity structure are accounted for (e.g., Maggi et al., 2000). This depth is slightly shallower than the estimate of 8 km $\pm$ 3 km of Anderson & Webb (1989), but is based on modelled P and S waveforms rather than P waveforms alone, and is therefore better constrained. On a northwest dipping fault, this centroid depth and epicenter location (Fig. 2a) imply the primary slip occurred and initiated on the Edgecumbe fault rather than the other faults with surface rupture (Anderson et al., 1990). The base of the seismogenic crust is thought to be between 6 and 8 km depth in within the Whakatāne graben, based on ongoing seismicity and 1987 Edgecumbe earthquake aftershock locations (Beanland et al., 1990; Bryan et al., 1999; Robinson, 1989; Taylor et al., 2004). Therefore, we allow the base of the modelled Edgecumbe fault to reach between 6 and 8 km depth, overlapping with both focal mechanism and brittle crustal depths. We aimed for a fault base projection that extended horizontally 9 ± 3 km away from the Edgecumbe fault surface trace to maintain consistency with epicenter location and uncertainty from Anderson and Webb (1989).

Fault dip in the shallow subsurface is constrained by surface measurements of heave and throw from this study (see section 3.5 Horizontal displacements and coseismic heave). In the

Rangitāiki Plains, the near-horizontal and planar surface means that vertical separation can be used as a proxy for throw. We average groups of vertical separation measurements along the Edgecumbe fault over the same spatial extent as the horizontal vector groups. The combined heave, throw, and normal rake (-90°) yields a dip of ~65° for the Edgecumbe fault near the surface, which we project to 1 km depth (Table S3).

Constraining fault dip at depth is complicated by shallow seismic and gravity survey penetration, degraded resolution with depth, and poorly constrained changes in material velocities. The interpretations of seismic and gravity surveys suggest that the Edgecumbe fault dips steeply (~60°) in the upper 1 to 2 km of the crust (Mouslopoulou et al., 2008). This depth coincides with the depth of alluvial cover above more coherent Matihana ignimbrite and greywacke basement rock (Mouslopoulou et al., 2008) which could influence a change in fault dip as the plane approaches the surface and refracts in differing material (Bray et al., 1994). Focal mechanisms of the Edgecumbe mainshock suggest fault dips of 32 +5/-10° (Webb & Anderson, 1998) or 45 ± 10° (H. Anderson & Webb, 1989). We prefer the lower dip angle estimate of Webb & Anderson (1998) because it is based on more data, including modeled S seismograms that were absent from the earlier analysis of H. Anderson & Webb (1989). Additionally, in order for the Edgecumbe fault to reach both 7 ± 1 km depth and extend 9 ± 3 km away horizontally from the surface trace, the fault dip must be significantly less at depth than at the surface (65° calculated here). We therefore vary fault dips in the deeper crust to fit these constraints, between ~30° and ~55°, allowing for steeper dips in the shallower crust.

Finally, we vary slip along the modelled fault plane (both along strike and at depth) to approximately match measured scarp vertical separations from this study, relative patterns of vertical motion from the vertical difference model, and relative vertical movements from post-earthquake levelling surveys (Blick & Flaherty, 1989). In the final model we also aim for a moment magnitude between 6.4 and 6.6, based on estimations from long-period body-wave modelling (H. Anderson & Webb, 1989; Webb & Anderson, 1998). To aid with observed and modelled comparisons, we created a smoothed map of the SfM-based vertical difference model. This smoothed surface model is resampled using median values over a 1 km wide moving window in order to remove some of the high-frequency artifacts and create simplified deformation contours. The smoothed vertical difference model was also manually shifted up 0.5 m in elevation, uniformly, to try and match field observations that suggest little to no vertical deformation near the Rangitāiki Plains margin or in the majority of the Edgecumbe fault footwall (Blick & Flaherty, 1989) (Fig. S3).

4 Vertical difference model and fault mapping

Our SfM-based vertical difference model, DSMs, and orthomosaics were used to map and measure coseismic displacement. The pre- and post-event models produced DSMs with resolutions up to 68.4 cm and 30.7 cm grid size, respectively, and orthomosaics of 34.2 cm and 15.3 cm pixels, respectively (See Open Data). The down-sampled 2 m datasets were typically more useful because high-frequency noise from model artifacts is reduced (Fig. 2a).

We could typically measure displacements along fault traces with ≥ 0.3 m of vertical separation along discrete faults (Figs. 2, 5). In some instances, fault traces with ≤ 0.3 m vertical separations were mapped but we could not make accurate measurements within the vertical difference model due to noise that exceeded displacements. An important caveat is that this method, at the resolution of these photos, cannot distinguish shallow blind faulting from surface

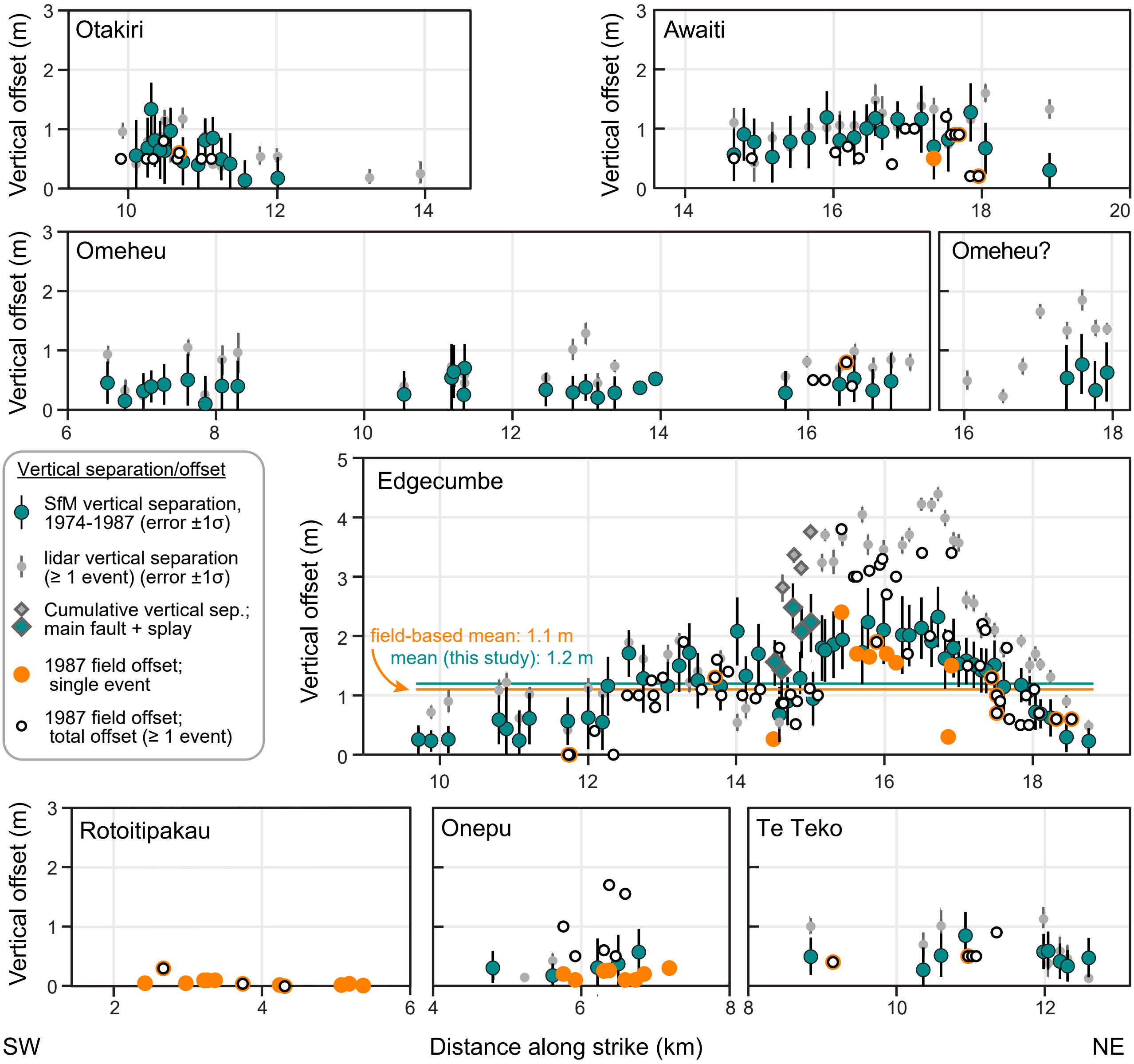

Figure 5: Vertical separations and offsets along fault segments measured from the vertical difference model compared to 1987 field-based measurements (Beanland et al., 1989) and lidar-based measurements (this study). Uncertainties from field measurements were not reported. All values are projected to the strike line (see Fig. 3). Our SfM-based measurements typically agree well with and are denser than the field measurements, but are unable to resolve very small displacements (e.g., the Rotoitipakau fault). Lidar-based measurements confirm that the SfM measurements capture only single-event displacement, compared to the 1987 total offsets (white circles) which may be single or multi-event.

rupture where the fault breaks the surface. Therefore, we refer to any localized tectonic surface deformation along mapped fault traces as surface rupture, though some may be fold scarps.

We mapped a cumulative ~50 km of certain, approximate, and possible fault traces that ruptured in the 1987 Edgecumbe earthquake (Fig. 2b). These traces were named largely according to existing fault mapping (Begg & Mouslopoulou, 2010), but in some instances, the density of minor fault traces, changes in apparent dip, and unknown geometry at depth make name classification difficult (e.g., the Omeheu and Otakiri faults) (Fig. 2b).

We were able to identify all fault traces that were mapped in 1987 except the Rotoitipakau fault zone (Fig. 2b). Additionally, ~32 km of fault traces mapped in this study were not identified in 1987, though these are typically lower confidence and low-amplitude scarps. By comparing the pre-earthquake images and surface models to the vertical difference model, we observed that all mapped fault zones that ruptured in 1987 (Edgecumbe, Awaiti, Te Teko, Omeheu, Otakiri, and Onepu faults) had sections with pre-existing scarps (See mapping in Data Repository).

We measured coseismic vertical displacement at 132 sites along fault scarps by extracting swath profiles from the vertical difference model (Figs. 3, 4, 5). The maximum vertical separation measured is 2.5 ± 0.4 m, which combines slip on the main Edgecumbe fault and the small splay near the fault center (Fig. 5). The lower limit of measured vertical separations (~0.25–0.3 m) have one standard deviation that is as large as or larger than the vertical separation, which is expected due to the high noise of the pre-earthquake DSM.

The swath profiles also inform the surface displacement wavelength due to slip on individual fault strands. For example, subsidence in the Edgecumbe and Awaiti fault hanging walls is not fully recovered over the 500 m visible in the profile, but slip on the other structures, such as the Omeheu and Otakiri faults, is often recovered within 200–500 m away from the fault (Fig. 4). This wavelength has implications for the fault geometry and slip distribution, and is discussed below.

Manually drawn vectors measurements adjacent to the central Edgecumbe fault on the pre- and post-earthquake orthophoto mosaics yielded 21 relative horizontal displacement vectors on the hanging wall and 17 relative horizontal displacement vectors on the footwall (Fig. S1; see Open Data). The hanging wall and footwall vectors were split into three spatial groups to produce average coseismic heave values of 0.9 m, 1.0 m, and 0.7 m (Fig. S1, Table S3). When combined with nearby vertical separation measurements, these heave values correspond to near-surface fault dips of 64°, 64°, and 65°, respectively (Table S3).

5 Sources of difference model error and implications for measurements

The post-earthquake photoset generated a minimally distorted DSM due to the ideal camera lens, short duration of survey time, photo overlap, and low flight altitude. The pre-earthquake photo set and resulting DSM is lower resolution (68 cm versus 31 cm for the post-earthquake DSM) and contains more artifacts; therefore, the pre-event SfM model is the primary source of distortion in the vertical difference model (Fig. 2a). The pre- and post-earthquake DSMs have the largest artifacts (distortion) in three major areas: (i) the coastline, (i) between flight lines, and (iii) along the model edges. Minor artifacts are also present between individual photos along the seams. These distortions manifest as topographic breaks that are aligned due east-west (parallel to photograph orientations and flight paths) or as long wavelength undulations and doming that do not reflect realistic landscape changes, and are most apparent when comparing the DSMs (pre and post-earthquake) to the lidar DEM (Fig. S2).

Doming is a known problem common to photogrammetry (e.g., Zhou et al., 2016) and is typically mitigated with additional control points, but several problems limit that solution in this study. First, outside of the Rangitāiki Plains, the region is heavily forested and repeatedly clear-cut. Dense vegetation typically poorly aligns in Agisoft Metashape Pro; here we suspect that the tree canopy and associated shadows provide few opportunities for unique model tie points (tie points are used in photo alignment). Oscillation between forest cover and clear-cut land also reduces the locations available for reliable and consistent control points. Second, previous post-earthquake levelling surveys identified that much of the coast and Rangitāiki Plains either subsided or slightly uplifted during the earthquake, or experienced fluctuations due to groundwater withdrawal over longer periods (Blick & Flaherty, 1989). Therefore, most of the Rangitāiki Plains and coastline in the SfM-based models do not contain reliable control points. Finally, large artifacts exist in the pre-earthquake model along flight lines (Fig. 2a). These artifacts were partially reduced, but not eliminated, by including non-georeferenced check points within Agisoft (see Methods). Ultimately, flight line problems originate from poor photo overlap, photo vignetting, and the long photo set collection duration and therefore are unlikely to be completely removed from this photoset without significant photo or model post-processing.

The artifacts and inaccuracies in these SfM-based models have several implications for the resulting vertical difference model. First, long wavelength vertical model warping exists over the many-kilometer-scale (~5 km).While some long-wavelength tectonic deformation likely occurred (e.g., Blick and Flaherty, 1989), we cannot necessarily separate these tectonic signals from SfM artifacts. Second, apparent elevation changes across flight lines, or less prominently, across photo seams, must be avoided when measuring coseismic vertical separation. Finally, the relatively widely spaced geographic control, long wavelength warping, and more discrete artifacts along photo and flight line seams mean that the difference values at any given point (from the vertical difference models) are likely not representative of absolute coseismic vertical change. This is apparent when comparing field-levelling data to the difference model (Fig. S3). For example, large swaths of land southwest of Te Teko did not apparently move in the Edgecumbe earthquake or minorly subsided (Blick & Flaherty, 1989), but appear to have uniformly uplifted in the vertical difference model (Fig. 2, S3). We therefore consider relative elevation changes across short distances (<2 km), such as taken in fault profiles (Fig. 4), to be reliable measures of coseismic deformation. Wider scale deformation patterns are useful to consider in a general sense but may reflect coseismic deformation less accurately.

6 Comparison of displacement measurements with field observations

The use of photogrammetry techniques with aerial photos to build pre- and post-earthquake topographic datasets is a relatively new technique that has only sparsely been applied to coseismic displacement measurements (e.g., Howell et al., 2020; Zhou et al., 2016), and is typically used on larger magnitude events with bigger displacements. In order to understand the strengths, weaknesses, and limitations of this technique, it is important to compare the results of SfM-based surface models and measurements to other data collected with established techniques such as field surveys and lidar-based measurements.

The 1987 field-based along-fault measurements fell into two categories: single event vertical offsets from the 1987 earthquake, and total scarp vertical offsets (Beanland et al., 1989)

(Fig 3b, 5; digitized in Table S4). The term "offset" is used in field-based studies and we keep that terminology here—these on-fault measurements may not capture full vertical separation. In some locations, where a reliable displaced marker was present, both single event and total vertical offset were measured (Beanland et al., 1989). Without information about pre-earthquake topography, these total vertical offsets may represent either displacement only from the 1987 earthquake or multi-event displacement. Beanland et al. (1989) identified pre-existing scarps where a 1987 offset and a larger total scarp height were measured at the same place.

Our coseismic vertical separation measurements generally agree with the field-based measurements (both 1987 single event and total offsets) along the flanks of the Edgecumbe fault and the Otakiri, Awaiti, Omeheu, Onepu, and Te Teko faults (Fig. 4 profile A; Fig. 5). An implication of this agreement is that the majority of the total offset field measurements likely only represent 1987 coseismic displacement. Many of our vertical separation values elsewhere are slightly larger than the field estimates when measured in the same location (Fig. 5), likely due to the longer profile length and ability to capture the full extent of vertical separation (Fig. 4).

Field-based studies identified three faults that ruptured in 1987 and had pre-existing scarps: the central Edgecumbe fault, the Onepu fault, and the Rotoitipakau fault zone (Fig. 2). Of the 1987 rupture traces mapped here, we identified pre-existing scarps on the central Edgecumbe, Onepu, Te Teko, Omeheu, and sections of the Otakiri faults based on the pre-earthquake DSM, expanding the record of multi-event scarps (See Open Data). We could not identify the small (~10-cm-high) coseismic displacements on the Rotoitipakau fault zone, but lineaments and pre-existing scarps along these fault traces are clearly visible in the pre-earthquake DSM topography, as identified by the field investigations (Beanland et al., 1989). On the central Edgecumbe fault, our vertical separation measurements are similar to field-based 1987 vertical offsets and significantly smaller (~0.9–1.3 m smaller) than a cluster of large (>2 m) total scarp height measurements (15.3–17.4 km on Fig. 5). This agrees well with previous pre-existing scarp height estimates (0.9–1.3 m) and indicates that the SfM-based vertical difference model is capturing only coseismic slip rather than cumulative scarp height.

We estimated average heave values of 0.7, 0.9, and 1.0 m near the central Edgecumbe fault, which is broadly consistent with field-based extensional measurements of 0.4–1.6 in the same region. Beanland et al. (1989) estimated a near-surface fault dip of 55°, which is less than our estimated value of ~65°. Our slightly larger single event vertical separation values account for the slightly steeper dip.

Based on field measurements, Beanland et al. (1989) calculated an average vertical offset along the Edgecumbe fault of 1.4 m. However, this value simply averages both 1987-only and total offset measurements and does not consider variation in measurement density along the rupture length, which may favor larger, more easily identified offset sites. To try to address these two issues, and to compare to results from this study, we recalculated the average field-based vertical offset by subsampling the likely 1987 offsets.

Our vertical offset/separations mean uses regularly-spaced, 1-km-wide moving-window averages taken every 200 m along the strike distance (see Fig. 3 for strike distance). The SfM-based moving window means are inversely weighted by the σ2 value while field measurements are weighted equally since they do not have error values. The final mean displacement value for the Edgecumbe fault is the average of all moving window means for that dataset. The recalculated 1987 field-based displacements include total vertical and 1987 vertical offsets (as reported by Beanland et al., 1987), but excludes offsets >2.5 m (likely multi-event) or clusters identified elsewhere as pre-existing scarp height (e.g., 15.3–17.4 km on Fig. 5) (Table S5). The average vertical displacement along the Edgecumbe fault is 1.2 m for field offsets and 1.5 m for SfM-based vertical separations over the field-measured fault length. Using the SfM-measured fault length, which is ~2.5 km longer than mapped in the field (Fig. 2b), field vertical offsets average 1.1 m and SfM vertical separations average 1.2 m (Fig. 5). These slightly larger average displacement values over the same distances suggest that this SfM-based method captures the full vertical separation (both away from the fault and along strike) better than the 1987 field measurements.

The average vertical displacement values above differ from the 0.6 m reported by Wesnousky (2008), which was incorporated into a global catalog to evaluate potential relationships between earthquake characteristics (e.g., length, slip, fault width, moment release). Wesnousky (2008) calculated average displacement by interpolating all offsets from Beanland et al. (1989) along the entire surface rupture length (15.5 km), rather than just the Edgecumbe fault trace. We avoided that approach here because the apparently shallow slip depths associated with the secondary faults may not be appropriate or comparable across a global earthquake catalog.

7 Elastic dislocation modelling and implications

Our new mapping and displacement data provide additional information about fault structure and slip behavior, warranting revisitation of the 1987 Edgecumbe earthquake fault model. Our preferred elastic dislocation model of the 1987 Edgecumbe earthquake includes slip on the Edgecumbe and Awaiti faults (Fig 6). The modeled Edgecumbe fault consists of an 8.5-km-long structure striking 240° with dips of 65° from 0 to 1 km depth, 50° from 1 to 2 km depth, and 35° from 2 to 7 km depth (Fig. 6; Table 1). The Awaiti fault was modelled as a 2.7-km-long planar fault striking 228° that dips 60° between 0 and 3 km depth. We find that the regional displacement field can be approximated with a peak slip of 4.5 m at depths 2 to 6 km along the Edgecumbe fault and 1.5 m peak slip along the Awaiti fault (Fig. 6, Table 1). Both faults include a pronounced tapered slip distribution along strike, with peak slip near the center of each fault (Fig. 6, Table 1). Slip on the Edgecumbe fault also includes a slight slip taper near the upper and lower fault edges. This fault geometry and prescribed slip yields an earthquake with M_w 6.54 (Hanks & Kanamori, 1979).

Table 1. Elastic dislocation fault parameters

Fault name	Depth range	Dip (°)	Normal slip (m) on modelled section From north to south				
Edgecumbe	0–1 km	65	1.5	3.0	2.5	1.0	0.5
	1–2 km	50	1.5	3.5	3.0	1.0	0.5
	2–6 km	35	2.0	4.5	3.5	1.5	0.5
	6–7 km	35	1.5	3.0	2.5	1.0	0.5
Awaiti	0–3 km	60	0.5	1.5	1.5	1.5	0.5

Table 1. Slip on the Edgecumbe and Awaiti faults used in the elastic dislocation modelling. Location of faults shown in Fig. 6. All slip has a pure normal rake (-90°).

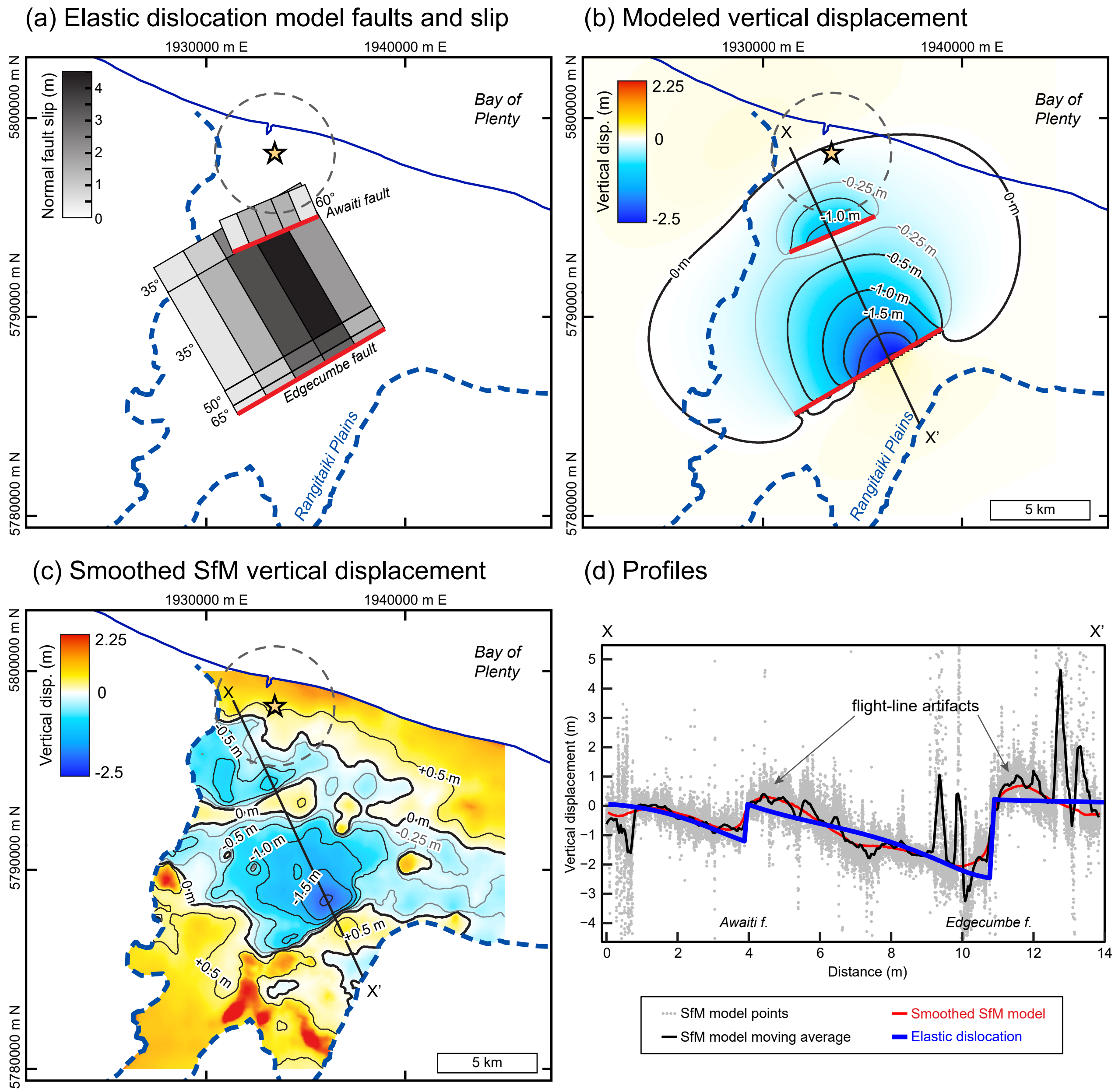

Figure 6: Comparison of elastic dislocation model slip and surface deformation to SfM-based vertical displacement of the 1987 Edgecumbe earthquake. Epicenter location (star) and uncertainty (dashed grey circle) from Anderson and Webb (1989). (a) Location and slip on the simplified Edgecumbe and Awaiti faults used in elastic dislocation modeling. Dip values labelled per segment row. Slip is tapered along strike and near fault edges (see Table 1). (b) Vertical surface displacement from the model shown in (a). Very little uplift (<0.25 m) is predicted. (c) Vertical displacement from the smoothed SfM-based vertical difference model, which is smoothed over a 1-km-moving-median window and trimmed to the Rangitāiki Plains extent. Most uplift is likely an artifact from poor photo overlap between frames and flight lines (see Fig. 2) and other problems described in the text. All values have been shifted up by 0.5 m to correct for lack of geographic control within the graben and flight line distortion. (d) Graben profiles comparing vertical difference model from Fig. 2a (shifted up 0.5 m), moving average of the vertical difference model, smoothed vertical difference model from (c), and the elastic dislocation model vertical displacement from (b). Black contour interval is 0.5 m; grey contour is -0.25 m.

We do not include other mapped fault traces in the final elastic dislocation model because they did not significantly alter the fit of observed and modelled displacements. Slip on these structures only extends up to ~500 m away from the fault trace at the surface (e.g., Fig. 4e). Elastic dislocation modelling suggests this short-wavelength vertical deformation can only be caused by slip less than 1 km below the surface, even with a range of plausible dip values (35-70°). Thus, we infer that these faults (i) likely did not host substantial slip at depth, (ii) did not link at depth with other 'seismogenic' faults during this earthquake, and (iii) did not contribute significant moment release during the 1987 earthquake.

The Edgecumbe fault dip at depth was most controlled by the estimated focal mechanism dip and location, both of which required a relatively gentle dip near the base of a thin seismogenic crust (H. Anderson & Webb, 1989; Webb & Anderson, 1998). While the hypocenter location is poorly constrained, the overall pattern of broad subsidence (Fig. 2; Fig. 6c), steep near-surface fault dip (Beanland et al., 1989; this study), little to no footwall uplift (Blick & Flaherty, 1989; this study), and a thin (6- to 8-km-thick) brittle crust (Robinson, 1989) is most simply accommodated by a gently dipping fault that steepens in the shallow subsurface (Fig. 6).

Our preferred model geometry implies the Edgecumbe fault is a relatively low-angle, normal fault for most of its area. At >2 km depths, our modelled dip (35°) is similar to previous elastic dislocation model dip estimates of 40°, which were based on relative horizontal displacements acquired from triangulation networks (Darby, 1989). Listric geometry of the Edgecumbe fault was previously discounted, despite surface dips significantly steeper than estimated subsurface dips (Beanland et al., 1990). It is unclear whether the Edgecumbe fault is truly listric (i.e., smooth decrease in dip with depth) or whether steeper fault dips only occur in the very near surface (<1 km) with a largely planar fault geometry below. In the case of the latter, near-surface dip changes could be due to surface crust failing under tension, consistent with dominantly planar geometry observed in other active normal faults (e.g., Reynolds & Copley, 2018). For the Edgecumbe fault, these semantics do not have much impact on the overall rupture area, moment release, or expected seismic hazard since the seismogenic crust is fairly thin and changes in dip likely occur within the upper few kilometers of the crust in either case.

Lower angle normal faults do not fit traditional Andersonian theory (E. M. Anderson, 1951), but 35° does fall within the observed dip range of 30-60° observed globally on normal faults (Collettini & Sibson, 2001; Jackson, 1987; Middleton et al., 2016; Reynolds & Copley, 2018; Wernicke, 1995). The fault hosting the M_w 5.7 2020 Magna earthquake in Utah, U.S.A., was inferred to have a similar geometry to our preferred Edgecumbe fault model; focal mechanisms suggest a gently dipping (20–32°) fault plane at depth that steepens to 70° near the surface, though no surface rupture was observed in that event (Pang et al., 2020). The Edgecumbe earthquake can thus provide an important case study of rupture behavior and surface deformation patterns when gently-dipping normal faults rupture to the surface through the width of the seismogenic crust.

Previously inferred dips on TVZ faults are steeper (~60°) as a compromise between gentler estimated deep fault dips and steep surface dips (Villamor & Berryman, 2001). If, like the Edgecumbe fault, the majority of TVZ faults have lower dip angles for the majority of their area, this could influence both slip rate and earthquake size estimates for the region. Alternatively, the

Edgecumbe fault may have lower overall dip values than the average Taupō rift fault because it is a primary graben-bounding structure that has rotated farther from an initially steeper dip (e.g., Jackson, 1987). More information about fault dips at depths > 1 km is needed to understand these relationships.

It is important to note that while our preferred model of the 1987 earthquake is generally a good fit to surface and seismological observations, it is not a unique solution. Similar models with slightly different fault geometries (e.g., depth, dip angles, and curvature) or slip distributions may fit the observations similarly as well. Broadly speaking, however, significantly different and new information about the subsurface geometry or hypocenter location would be required to greatly change the inferred fault behavior. The most significant differences between our elastic dislocation modelling and the previous model of Darby (1989) are a heterogeneous slip distribution informed by a denser network of surface displacement observations, a slightly gentler fault dip, a spatially variable fault orientation made possible by improvements in software, and the addition of the Awaiti fault.

8 Pushing the limits: lessons learned in reconstructing moderate magnitude earthquake deformation fields from historical imagery

This study has two main foci: (1) the development of a new technique using historical air photos to build pre- and post-earthquake surface models, and (2) the implications of our results for Edgecumbe area and interactions in TVZ. We therefore separate our discussion by focusing first on the application of our method and second on the tectonics in the Rangitāiki Plains.

8.1 Advantages and limitations of surface displacement measurements from historical aerial images

We have shown that using historical aerial photos to generate digital surface models can be an effective and useful technique, particularly in the absence of other high-resolution topographic data. The primary advantages include the abilities to (1) take dense measurements and fill in spatial gaps from previous surveys, (2) measure displacements across a wide aperture, including distributed deformation and off-fault displacement, (3) identify subtle deformation that is difficult to identify on the ground, such as along small or blind fault and fold scarps, (4) discern between new fault scarps and pre-existing fault scarps, and (5) estimate the depth of faulting based on surface deformation width. In this study, we resolved vertical deformation confidently to ~0.3 m in our difference model (Fig. 5). We located nearly all of the fault traces mapped in post-earthquake reconnaissance, and in some cases, mapped traces that were not identified following the earthquake (Fig. 2). The newly-mapped 1987 rupture traces are typically extensions of known scarps, or wide, low-amplitude (<0.5 m) scarps several hundreds of meters from other mapped fault traces. The newly mapped fault traces may represent fold scarps across a locally blind, shallow fault, though we cannot distinguish folds from fault scarps using this method. In the absence of surface cracking, discrete breaks from surface rupture, or obviously deformed cultural markers, these scarps would be very difficult to detect in the field.

The limitations and challenges of this technique depend on the geographic setting and photosets, but generally include (1) artifacts from flight lines, (2) long wavelength warping, and (3) limitation to the final product resolution. Ultimately, the quality of an SfM-derived DSM is highly dependent on the resolution and quality of the photoset used to generate the model. In other words, factors such as high flight altitude, poor photo overlap (<60%), too short or too long lens focal lengths, presence of clouds or harsh shadows, photo vignetteing, and time over which photos were taken will all negatively impact the SfM model generation process. In this study, these problems were highlighted by the difference in final model quality between the pre-earthquake and post-earthquake SfM-based DSMs—the 1987 post-earthquake photos generated a much clearer, lower-noise, and higher resolution DSM than the pre-earthquake photos. The Rotoitipakau fault zone could not be mapped using the SfM-based method (Fig. 2b) due to a combination of prominent model warping artifacts and very small displacements of ~10 cm (Beanland et al., 1989). Combined with findings described above of newly mapped fault traces, this suggests that there may be other 1987-activated fault traces with small vertical separations (<30 cm) that remain undocumented by either field mapping or SfM difference mapping, particularly if brittle deformation at the surface was absent. Precise independent ground control, if available, can reduce some model artifacts, but errors introduced during model generation (e.g., warping between control points) can be difficult to quantify (Delano et al., 2021).

We were unable to accurately resolve the effects of tectonic subsidence from sediment compaction and other non-tectonic processes in this study. Broad-scale sediment compaction in unconsolidated alluvial fill and pore water movement was documented to some extent post-earthquake, but was poorly constrained and likely spatially heterogeneous due to variable sediment deposits and groundwater distribution (Blick & Flaherty, 1989). Where measured, the vertical effects of sediment compaction were ~0.2–0.3 m (Blick & Flaherty, 1989; Pender & Robertson, 1987), which is generally less than one standard deviation of our displacement measurements. Untangling non-tectonic ground deformation at this scale from tectonic displacement is a challenge that extends beyond this study and method. Accurately quantifying non-tectonic processes would require more information on subsurface materials and properties, and some form control that can be compared before and after the earthquake.

8.2 Role of minor faults during coseismic deformation

The Edgecumbe earthquake is a moderate magnitude (M_w 6.5) earthquake that has a short primary fault rupture length (i.e., the Edgecumbe fault) compared to average and maximum slip, high degree of secondary faulting, and a very wide faulted zone compared to global catalogs of normal fault earthquakes (Ferrario & Livio, 2021; Wesnousky, 2008). Our additional fault trace mapping only increases these values—secondary faulting is denser than previously recognized, increasing the amount of distributed faulting for this event (Ferrario & Livio, 2021). Based on our mapping combined with the Rotoitipakau fault traces from Beanland et al. (1989), there were 17.6 km of primary fault (Edgecumbe and Awaiti) surface rupture traces and 36.8 km of secondary fault surface rupture traces (Fig. 2b). If we consider only the certain and approximate traces, these values are 15.9 km (38%) for primary and 25.9 km (62%) for secondary traces. Most other well-studied historical normal fault ruptures, such as those in the western U.S., produced more localized fault rupture along narrower zones than observed here (e.g., Caskey et al., 1996; DuRoss et al., 2019; Wallace et al., 2004). Therefore, the significant secondary surface rupture seen during the Edgecumbe earthquake may be more representative of backarc normal fault events, such as the M_w 6.5 2016 Central Italy earthquake, which also produced a wide zone of faulting with similar peak slip and complex reactivation of existing faults (Ferrario & Livio, 2018).

Surface deformation on secondary structures, which likely did not have significant slip at depth or contribute to seismic moment, is important from a fault displacement hazard perspective

(ANSI/ANS, 2015; Ferrario & Livio, 2018). For example, during the 2016 Kaikōura earthquake, minor surface slip occurred on the Hope fault without apparent slip at depth, causing road damage and suggesting that this phenomenon may be common at least in New Zealand earthquakes (Litchfield et al., 2018). Complex and distributed surface rupture and the hazard due to coseismic surface displacement may not be captured by only concentrating on traditional metrics such as magnitude, fault length, and peak or average slip, or fault zone width. The observation that secondary structures produced a surface scarp without slip at depth also has important implications for interpreting paleoseismic records. If scarp production does not necessarily correlate to seismogenic slip at depth, the interpreted paleoseismic record from trenches in these types of settings becomes more complicated. In the case of the Rangitāiki Plains, past interpretation of the number paleoearthquakes assumes primary rupture for many scarps, which without extensive timing data could lead to an overestimation of earthquake frequency (Begg & Mouslopoulou, 2010).

8.3 Possible magma-tectonic interactions in the Rangitāiki plains

Understanding the complex interactions between magmatic and seismic activity is critical to characterizing both volcanic and earthquake hazard in active rift settings like the TVZ. The 1987 Edgecumbe earthquake is generally considered an amagmatic earthquake within the tectonically-dominated northern TVZ (Rowland et al., 2010). Hamling et al. (2016), however, demonstrated that an inflating sill at depth along the western margin of the Rangitāiki Plains may control longer term uplift and could produce stress changes that promoted earthquakes like the 2005-2009 Matatā sequence.

The Edgecumbe earthquake was preceded by foreshocks that extended northeast of the mainshock (Fig. 1) (Smith & Oppenheimer, 1989). This foreshock cluster occurred in a similar location to (~10 km farther west) and along trend with the 2005-2009 Matatā sequence. Importantly, the edge of the best fit sill location determined by Hamling et al. (2016) coincides with the approximate hypocenter of the 1987 Edgecumbe earthquake (Fig. 7a). The similarity between the Edgecumbe and the Matatā sequences leads to the question: could the Edgecumbe earthquake sequence have been triggered by stress changes from the inferred inflating sill below Matatā?

We explored the idea of magma-inflation-triggered earthquakes within the Whakatāne graben by modelling the sill geometry and inflation used in Hamling et al. (2016) and imposing the resulting static stress on simplified versions of the Edgecumbe fault, Awaiti fault, and approximate planar fit to 1987 foreshock cluster (Fig 7). We lack focal mechanism or hypocenter data for the foreshock cluster events, but model the foreshock swarm as a southwest-striking, 45° northwest-dipping plane similar to other offshore central Whakatāne graben faults (Fig. 1b, Fig. 7) (Lamarche et al., 2006). We modelled a range of plausible sill locations, extents, and depths based on values and uncertainties from Hamling et al. (2016). Sill inflation was fixed to 1 m, which represents an inflation rate of 20 mm/yr over 50 years (Hamling et al., 2016). Coulomb stress change was calculated in Coulomb v3.3, assuming a pure normal slip (rake of -90°) (Toda et al., 2011).

Depending on the location and depth of the sill, the imposed sill inflation causes static stress changes that either promote or inhibit slip on portions of the simplified faults. In general, positive stress changes occur with two sill configurations: (1) when the sill and fault bases are at similar depths and the sill is northwest of the fault bases, slip is promoted at the base of the

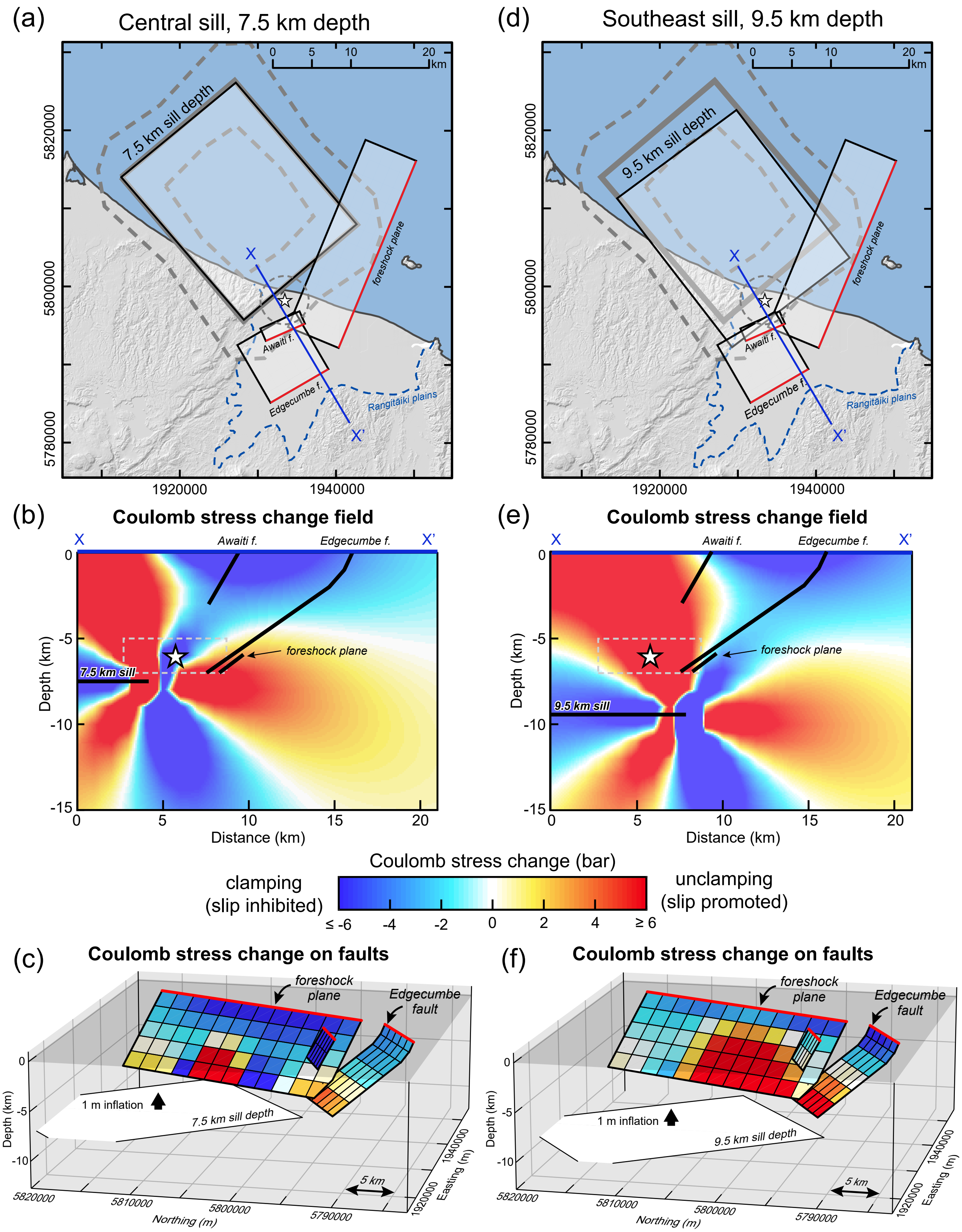

Figure 7: Stress changes on faults involved in the Edgecumbe earthquake sequence caused by sill inflation. The best-fit sill location of Hamling et al. (2016) is shown by the solid grey rectangle, location uncertainty shown by thick dashed grey polygons, and depth reported as 9.5 km ± 2.1 km. The Edgecumbe and Awaiti faults are the same as in Fig. 6, but further partitioned into patches <2.5 x 2.5 km. The foreshock plane follows the trend of 1987 foreshocks with a 45° dip. Epicenter (star) location and uncertainty (thin grey dash) from Anderson and Webb (1989); depth and associated uncertainty is from Webb and Anderson (1998). Sill inflation of 1 m based on 20 mm/yr over 50 years (Hamling et al., 2016). (a–c) Location of modeled faults and modeled stress changes for a central sill location at 7.5 km depth. The base of the Edgecumbe and foreshock fault planes have zones of increased Coulomb stress. (d–f) Location of modeled faults and modeled stress changes for a southeastern sill at 9.5 km depth. Large portions of the base of the Edgecumbe, foreshock, and Awaiti faults occur in zones of Coulomb stress increases. Both configurations are examples where sill inflation promotes slip near the observed 1987 foreshocks and mainshock epicenter and centroid depth. In (b) and (e), stress changes are relative to a fault with strike/dip/rake of 240/45/-90.

Edgecumbe and foreshock faults (Fig. 7a–7c), and (2) when the sill edge ends below a portion of modelled faults at any depth, slip is promoted at the base of all three faults (Edgecumbe, foreshock, and Awaiti planes) (Fig. 7d–7f).

The existence of reasonable sill inflation models that promote slip on these faults suggests a plausible scenario where as the sill inflates, slip is triggered at depth on favorably oriented nearby faults, as was inferred in the Matatā sequence by Hamling et al. (2016). Further, slip along the base of either the Edgecumbe or foreshock plane faults results in positive static stress changes that promote slip in both along-strike and up-dip directions. Earthquake rupture may then continue on to other structures, which may already be near failure, due to static or dynamic stress changes.

The TVZ contains many active faults (Fig. 1) with complex relationships to the underlying magmatic bodies and many mechanisms have been proposed for volcano- tectonic interactions and triggering (e.g., Rowland et al., 2010; Villamor et al., 2017; Wilson & Rowland, 2016). Though faulting in the Whakatāne graben and during the Edgecumbe earthquake is considered tectonic-dominated rather than magmatic-driven (H. Anderson et al., 1990; Rowland et al., 2010), it is possible that the timing of the 1987 Edgecumbe earthquake may have been advanced by the interaction with long-term sill inflation and the cascading influence of stress on adjacent faults.

5 Conclusions

We have demonstrated that historical aerial photos can be used to construct SfM-based pre and post-earthquake topographic models useful for detecting coseismic surface deformation. When applied to the M_w 6.6 1987 Edgecumbe earthquake in New Zealand, we find that our SfM-based measurements generally agree with, but are slightly larger than, field-based measurements. We also detected many more small, subtle scarps than were mapped in the field survey. As a result, our understanding of surface deformation associated with the Edgecumbe earthquake is improved by a far denser dataset of vertical displacement measurements, the ability to distinguish single-event displacement and pre-existing scarps, and the ability to assess change over a wider aperture to include off-fault deformation.

The improved surface displacement data constrain updated fault geometries and a new elastic dislocation model of the earthquake, which compared to earlier efforts, now includes tapered slip, gentler fault dips at depth, steep fault deps in the near surface, and the inclusion of the Awaiti fault. The 1987 Edgecumbe earthquake is somewhat unusual in the amount of surface rupture on dominantly secondary (non-seismogenic at depth) faults for a moderate-magnitude event. The prevalence of secondary structure surface rupture may be a result of the back-arc rift setting and thin seismogenic crust; such behavior should be taken into account in probabilistic surface displacement hazard assessments for this type of tectonic setting. Finally, we have shown that the Edgecumbe fault could have been pushed to rupture by stress changes associated with an inflating sill at depth. This finding suggests that the timing of moderate-large ‘tectonic’ earthquakes may be advanced by fault interaction with magmatic processes like sill inflation and the cascading influence of stress changes on adjacent faults.

Acknowledgments

We thank the reviewers for their contributions to improving the manuscript. Useful early discussion with David Napier, Graeme Blick, Pilar Villamour, Kelvin Berryman, and Andy Nicol helped guide the foundations of this research. Narges Khajavi provided preliminary fault trace mapping and digitized pre-existing mapping. This research was funded by the Mason Trust and QuakeCoRE.

Open Research

Aerial images used in this study were sourced from the LINZ Data Service and licensed by Crown Aerial Film Archive for reuse under the CC BY 4.0 license. Bay of Plenty lidar point clouds available from ftp://files.boprc.govt.nz/Public (accessible using Internet Explorer). The supplementary files include Figures S1-S4. The associated data repository includes shapefiles of 1987 rupture and reactivated scarp mapping, pre- and post-earthquake DSMs, and the difference model raster, and Tables S1-S4 (*in supplementary data during review*).

References

Abdullah, Q., Bethel, J., Hussain, M., & Munjy, R. (2013). Photogrammetric project and mission planning. Manual of Photogrammetry. American Society for Photogrammetry and Remote Sensing, 1187–1220.

Ambraseys, N. N. (1963). The Buyin-Zara (Iran) earthquake of September, 1962 a field report. Bulletin of the Seismological Society of America, 53(4), 705–740.

Anderson, E. M. (1951). The Dynamics of Faulting and Dyke Formation with Applications to Britain. New York: Hafner Publishing Company.

Anderson, H., & Webb, T. (1989). The rupture process of the 1987 Edgecumbe earthquake, New Zealand. New Zealand Journal of Geology and Geophysics, 32(1), 43–52. https://doi.org/10.1080/00288306.1989.10421387

Anderson, H., Smith, E., & Robinson, R. (1990). Normal faulting in a back arc basin: Seismological characteristics of the March 2, 1987, Edgecumbe, New Zealand, Earthquake. Journal of Geophysical Research, 95(B4), 4709. https://doi.org/10.1029/JB095iB04p04709

ANSI/ANS. (2015). ANSI/ANS-2.30: Criteria for assessing tectonic surface fault rupture and deformation at nuclear facilities. La Grange Park, IL: American Nuclear Society.

Beanland, S., Berryman, K. R., & Blick, G. H. (1989). Geological investigations of the 1987 Edgecumbe earthquake, New Zealand. New Zealand Journal of Geology and Geophysics, 32(1), 73–91. https://doi.org/10.1080/00288306.1989.10421390

Beanland, S., Blick, G. H., & Darby, D. J. (1990). Normal faulting in a back arc basin: Geological and geodetic characteristics of the 1987 Edgecumbe Earthquake, New Zealand. Journal of Geophysical Research: Solid Earth, 95(B4), 4693–4707. https://doi.org/10.1029/JB095iB04p04693

Begg, J. G., & Mouslopoulou, V. (2010). Analysis of late Holocene faulting within an active rift using lidar, Taupo Rift, New Zealand. Journal of Volcanology and Geothermal Research, 190(1–2), 152–167. https://doi.org/10.1016/j.jvolgeores.2009.06.001

Bemis, S. P., Micklethwaite, S., Turner, D., James, M. R., Akciz, S., Thiele, S. T., & Bangash, H. A. (2014). Ground-based and UAV-Based photogrammetry: A multi-scale, high-resolution mapping tool for structural geology and paleoseismology. Journal of Structural Geology, 69, 163–178. https://doi.org/10.1016/j.jsg.2014.10.007

Blick, G. H., & Flaherty, M. P. (1989). Regional vertical deformation associated with the 1987 Edgecumbe earthquake, New Zealand. New Zealand Journal of Geology and Geophysics, 32(1), 99–108. https://doi.org/10.1080/00288306.1989.10421392

Bray, J. D., Seed, R. B., Cluff, L. S., & Seed, H. B. (1994). Earthquake Fault Rupture Propagation through Soil. Journal of Geotechnical Engineering, 120(3), 543–561. https://doi.org/10.1061/(ASCE)0733-9410(1994)120:3(543)

Bryan, C. J., Sherburn, S., Bibby, H. M., Bannister, S. C., & Hurst, A. W. (1999). Shallow seismicity of the central Taupo Volcanic Zone, New Zealand: Its distribution and nature. New Zealand Journal of Geology and Geophysics, 42(4), 533–542. https://doi.org/10.1080/00288306.1999.9514859

Caskey, S. J., Wesnousky, S. G., Zhang, P., & Slemmons, D. B. (1996). Surface faulting of the 1954 Fairview Peak (MS 7.2) and Dixie Valley (MS 6.8) earthquakes, central Nevada. Bulletin of the Seismological Society of America, 86(3), 761–787. https://doi.org/10.1785/BSSA0860030761

Collettini, C., & Sibson, R. H. (2001). Normal faults, normal friction? Geology, 29(10), 927–930. https://doi.org/10.1130/0091-7613(2001)029<0927:NFNF>2.0.CO;2

Darby, D. J. (1989). Dislocation modelling of the 1987 Edgecumbe earthquake, New Zealand. New Zealand Journal of Geology and Geophysics, 32(1), 115–122. https://doi.org/10.1080/00288306.1989.10421394

Delano, J. E., Briggs, R. W., DuRoss, C. B., & Gold, R. D. (2021). Quick and Dirty (and Accurate) 3D Paleoseismic Trench Models Using Coded Scale Bars. Seismological Research Letters. https://doi.org/10.1785/0220200246

DuRoss, C. B., Bunds, M. P., Gold, R. D., Briggs, R. W., Reitman, N. G., Personius, S. F., & Toké, N. A. (2019). Variable normal-fault rupture behavior, northern Lost River fault zone, Idaho, USA. Geosphere, 15, 1–24. https://doi.org/10.1130/GES02096.1.

Elliott, J. R., Walters, R. J., & Wright, T. J. (2016). The role of space-based observation in understanding and responding to active tectonics and earthquakes. Nature Communications, 7(1), 13844. https://doi.org/10.1038/ncomms13844

Ferrario, M. F., & Livio, F. (2018). Characterizing the Distributed Faulting During the 30 October 2016, Central Italy Earthquake: A Reference for Fault Displacement Hazard Assessment. Tectonics, 37(5), 1256–1273. https://doi.org/10.1029/2017TC004935

Ferrario, M. F., & Livio, F. (2021). Conditional probability of distributed surface rupturing during normal-faulting earthquakes. Solid Earth, 12(5), 1197–1209. https://doi.org/10.5194/se-12-1197-2021

Hamling, I. J., Hreinsdóttir, S., Bannister, S., & Palmer, N. (2016). Off-axis magmatism along a subaerial back-arc rift: Observations from the Taupo Volcanic Zone, New Zealand. Science Advances, 2(6), e1600288. https://doi.org/10.1126/sciadv.1600288

Hanks, T. C., & Kanamori, H. (1979). A moment magnitude scale. Journal of Geophysical Research: Solid Earth, 84(B5), 2348–2350. https://doi.org/10.1029/JB084iB05p02348

Henderson, J. (1933). New Zealand Geological Survey : Map of the Napier District - Showing changes of level, pressure ridges, and earth rents. Earthquake of 3 February 1931 and later [facsimile]. Retrieved from https://ndhadeliver.natlib.govt.nz/delivery/DeliveryManagerServlet?dps_pid=IE57581309&dps_custom_att_1=emu

Howell, A. (2021). andy22b/fault-profile-tool: Fault profile tool (Version v0.1). Zenodo. https://doi.org/10.5281/ZENODO.5525497

Howell, A., Nissen, E., Stahl, T., Clark, K., Kearse, J., Van Dissen, R., et al. (2020). Three-Dimensional Surface Displacements During the 2016 M W 7.8 Kaikōura Earthquake

(New Zealand) From Photogrammetry-Derived Point Clouds. Journal of Geophysical Research: Solid Earth, 125(1). https://doi.org/10.1029/2019JB018739

Jackson, J. A. (1987). Active normal faulting and crustal extension. Geological Society, London, Special Publications, 28(1), 3–17. https://doi.org/10.1144/GSL.SP.1987.028.01.02

Johnson, K., Nissen, E., Saripalli, S., Arrowsmith, J. R., McGarey, P., Scharer, K., et al. (2014). Rapid mapping of ultrafine fault zone topography with structure from motion. Geosphere, 10(5), 969–986. https://doi.org/10.1130/GES01017.1

Kelsey, H. M., Hull, A. G., Cashman, S. M., Berryman, K. R., Cashman, P. H., Trexler, J. H., Jr., & Begg, J. G. (1998). Paleoseismology of an active reverse fault in a forearc setting: The Poukawa fault zone, Hikurangi forearc, New Zealand. GSA Bulletin, 110(9), 1123–1148. https://doi.org/10.1130/0016-7606(1998)110<1123:POAARF>2.3.CO;2

Koehler, R. D., Dee, S., Elliott, A., Hatem, A., Pickering, A., Pierce, I., & Seitz, G. (2021). Field Response and Surface-Rupture Characteristics of the 2020 M 6.5 Monte Cristo Range Earthquake, Central Walker Lane, Nevada. Seismological Research Letters, 92(2A), 823–839. https://doi.org/10.1785/0220200371

Krauss, K. (1993). Photogrammetry, Fundamentals and Standard Processes. Dümmlers Verlag, Bonn.

Lamarche, G., Barnes, P. M., & Bull, J. M. (2006). Faulting and extension rate over the last 20,000 years in the offshore Whakatane Graben, New Zealand continental shelf. Tectonics, 25(4). https://doi.org/10.1029/2005TC001886

Langridge, R., Ries, W., Litchfield, N., Villamor, P., Van Dissen, R., Barrell, D., et al. (2016). The New Zealand Active Faults Database. New Zealand Journal of Geology and Geophysics, 59(1), 86–96. https://doi.org/10.1080/00288306.2015.1112818

Leprince, S., Barbot, S., Ayoub, F., & Avouac, J.-P. (2007). Automatic and precise orthorectification, coregistration, and subpixel correlation of satellite images, application to ground deformation measurements. IEEE Transactions on Geoscience and Remote Sensing, 45(6), 1529–1558.

Litchfield, N. J., Villamor, P., Dissen, R. J. V., Nicol, A., Barnes, P. M., A. Barrell, D. J., et al. (2018). Surface Rupture of Multiple Crustal Faults in the 2016 M_w 7.8 Kaikōura, New Zealand, Earthquake. Bulletin of the Seismological Society of America, 108(3B), 1496–1520. https://doi.org/10.1785/0120170300

Lu, L., Zhou, Y., & Walker, R. T. (2021). Using historical aerial photographs to measure earthquake deformation: Testing the effects of scan resolution. Remote Sensing of Environment, 252, 112118. https://doi.org/10.1016/j.rse.2020.112118

Maggi, A., Jackson, J. A., Priestley, K., & Baker, C. (2000). A re-assessment of focal depth distributions in southern Iran, the Tien Shan and northern India: do earthquakes really occur in the continental mantle? Geophysical Journal International, 143(3), 629–661. https://doi.org/10.1046/j.1365-246X.2000.00254.x

Middleton, T. A., Walker, R. T., Parsons, B., Lei, Q., Zhou, Y., & Ren, Z. (2016). A major, intraplate, normal-faulting earthquake: The 1739 Yinchuan event in northern China. Journal of Geophysical Research: Solid Earth, 121(1), 293–320. https://doi.org/10.1002/2015JB012355

Mouslopoulou, V., Nicol, A., Little, T. A., & Walsh, J. J. (2007). Displacement transfer between intersecting regional strike-slip and extensional fault systems. Journal of Structural Geology, 29(1), 100–116. https://doi.org/10.1016/j.jsg.2006.08.002

Mouslopoulou, V., Nicol, A., Walsh, J. J., Beetham, D., & Stagpoole, V. (2008). Quaternary temporal stability of a regional strike-slip and rift fault intersection. Journal of Structural Geology, 30(4), 451–463. https://doi.org/10.1016/j.jsg.2007.12.005

Nissen, E., Krishnan, A. K., Arrowsmith, J. R., & Saripalli, S. (2012). Three-dimensional surface displacements and rotations from differencing pre- and post-earthquake LiDAR point clouds. Geophysical Research Letters, 39(16), n/a-n/a. https://doi.org/10.1029/2012GL052460

Nissen, E., Maruyama, T., Ramon Arrowsmith, J., Elliott, J. R., Krishnan, A. K., Oskin, M. E., & Saripalli, S. (2014). Coseismic fault zone deformation revealed with differential lidar: Examples from Japanese M_w ~7 intraplate earthquakes. Earth and Planetary Science Letters, 405, 244–256. https://doi.org/10.1016/j.epsl.2014.08.031

Ota, Y., Beanland, S., Berryman, K. R., & Nairn, I. A. (1988). The Matata Fault: Active faulting at the northwestern margin of the Whakatane Graben, eastern Bay of Plenty (New Zealand Geological Survey Record No. 35) (pp. 6–13).

Pang, G., Koper, K. D., Mesimeri, M., Pankow, K. L., Baker, B., Farrell, J., et al. (2020). Seismic Analysis of the 2020 Magna, Utah, Earthquake Sequence: Evidence for a Listric Wasatch Fault. Geophysical Research Letters, 47(18), e2020GL089798. https://doi.org/10.1029/2020GL089798

Pender, M. J., & Robertson, T. W. (Eds.). (1987). Edgecumbe Earthquake: Reconnaissance Report. Bulletin of the New Zealand National Society for Earthquake Engineering, 20, 201–249. https://doi.org/10.1193/1.1585452

Reitman, N. G., Bennett, S. E. K., Gold, R. D., Briggs, R. W., & DuRoss, C. B. (2015). High-Resolution Trench Photomosaics from Image-Based Modeling: Workflow and Error

Analysis. Bulletin of the Seismological Society of America, 105(5), 2354–2366. https://doi.org/10.1785/0120150041

Reynolds, K., & Copley, A. (2018). Seismological constraints on the down-dip shape of normal faults. Geophysical Journal International, 213(1), 534–560. https://doi.org/10.1093/gji/ggx432

Robinson, R. (1989). Aftershocks of the 1987 Edgecumbe earthquake, New Zealand: Seismological and structural studies using portable seismographs in the epicentral region. New Zealand Journal of Geology and Geophysics, 32(1), 61–72. https://doi.org/10.1080/00288306.1989.10421389

Rowland, J. V., Wilson, C. J. N., & Gravley, D. M. (2010). Spatial and temporal variations in magma-assisted rifting, Taupo Volcanic Zone, New Zealand. Journal of Volcanology and Geothermal Research, 190(1), 89–108. https://doi.org/10.1016/j.jvolgeores.2009.05.004

Schermer, E. R., Van Dissen, R., Berryman, K. R., Kelsey, H. M., & Cashman, S. M. (2004). Active faults, paleoseismology, and historical fault rupture in northern Wairarapa, North Island, New Zealand. New Zealand Journal of Geology and Geophysics, 47(1), 101–122. https://doi.org/10.1080/00288306.2004.9515040

Shao, Y., Liu-Zeng, J., Van der Woerd, J., Klinger, Y., Oskin, M. E., Zhang, J., et al. (2020). Late Pleistocene slip rate of the central Haiyuan fault constrained from optically stimulated luminescence, 14C, and cosmogenic isotope dating and high-resolution topography. GSA Bulletin, 133(7–8), 1347–1369. https://doi.org/10.1130/B35571.1

Smith, E. G. C., & Oppenheimer, C. M. M. (1989). The Edgecumbe earthquake sequence: 1987 February 21 to March 18. New Zealand Journal of Geology and Geophysics, 32(1), 31–42. https://doi.org/10.1080/00288306.1989.10421386

Taylor, S. K., Bull, J. M., Lamarche, G., & Barnes, P. M. (2004). Normal fault growth and linkage in the Whakatane Graben, New Zealand, during the last 1.3 Myr. Journal of Geophysical Research: Solid Earth, 109(B2). https://doi.org/10.1029/2003JB002412

Toda, S., Stein, R. S., Sevilgen, V., & Lin, J. (2011). Coulomb 3.3 Graphic-rich deformation and stress-change software for earthquake, tectonic, and volcano research and teaching—user guide (U.S. Geological Survey Open-File Report No. 2011–1060) (p. 63). Retrieved from t http://pubs.usgs.gov/of/2011/1060/

Villamor, P., & Berryman, K. (2001). A late Quaternary extension rate in the Taupo Volcanic Zone, New Zealand, derived from fault slip data. New Zealand Journal of Geology and Geophysics, 44(2), 243–269. https://doi.org/10.1080/00288306.2001.9514937

Villamor, P., Berryman, K. R., Ellis, S. M., Schreurs, G., Wallace, L. M., Leonard, G. S., et al. (2017). Rapid Evolution of Subduction-Related Continental Intraarc Rifts: The Taupo Rift, New Zealand: Rapid Evolution: Taupo Rift, New Zealand. Tectonics, 36(10), 2250–2272. https://doi.org/10.1002/2017TC004715

Wallace, L. M., Beavan, J., McCaffrey, R., & Darby, D. (2004). Subduction zone coupling and tectonic block rotations in the North Island, New Zealand. Journal of Geophysical Research: Solid Earth, 109(B12). https://doi.org/10.1029/2004JB003241

Webb, T. H., & Anderson, H. (1998). Focal mechanisms of large earthquakes in the North Island of New Zealand: slip partitioning at an oblique active margin. Geophysical Journal International, 134(1), 40–86. https://doi.org/10.1046/j.1365-246x.1998.00531.x

Wernicke, B. (1995). Low-angle normal faults and seismicity: A review. Journal of Geophysical Research: Solid Earth, 100(B10), 20159–20174. https://doi.org/10.1029/95JB01911

Wesnousky, S. G. (2008). Displacement and Geometrical Characteristics of Earthquake Surface Ruptures: Issues and Implications for Seismic-Hazard Analysis and the Process of Earthquake RuptureDisplacement and Geometrical Characteristics of Earthquake Surface Ruptures. Bulletin of the Seismological Society of America, 98(4), 1609–1632. https://doi.org/10.1785/0120070111

Wilson, C. J. N., & Rowland, J. V. (2016). The volcanic, magmatic and tectonic setting of the Taupo Volcanic Zone, New Zealand, reviewed from a geothermal perspective. Geothermics, 59, 168–187. https://doi.org/10.1016/j.geothermics.2015.06.013

Wilson, C. J. N., Houghton, B. F., McWilliams, M. O., Lanphere, M. A., Weaver, S. D., & Briggs, R. M. (1995). Volcanic and structural evolution of Taupo Volcanic Zone, New Zealand: a review. Journal of Volcanology and Geothermal Research, 68(1), 1–28. https://doi.org/10.1016/0377-0273(95)00006-G

Youngs, R. R., Arabasz, W. J., Anderson, R. E., Ramelli, A. R., Ake, J. P., Slemmons, D. B., et al. (2003). A Methodology for Probabilistic Fault Displacement Hazard Analysis (PFDHA). Earthquake Spectra, 19(1), 191–219. https://doi.org/10.1193/1.1542891

Zhou, Y., Walker, R. T., Hollingsworth, J., Talebian, M., Song, X., & Parsons, B. (2016). Coseismic and postseismic displacements from the 1978 M_w 7.3 Tabas-e-Golshan earthquake in eastern Iran. Earth and Planetary Science Letters, 452, 185–196. https://doi.org/10.1016/j.epsl.2016.07.038.